



## MAGNETOTELLURIC AND TRANSIENT ELECTROMAGNETIC METHODS IN GEOTHERMAL PROSPECTING, WITH EXAMPLES FROM MENENGAI, KENYA

**Peter Murabula Wameyo**

Kenya Electricity Generating Company - KenGen  
Geothermal Development Project,  
P.O. Box 785, Naivasha,  
KENYA  
*pwameyo@kengen.co.ke*

### ABSTRACT

Electromagnetic (EM) methods are used to determine variations in electrical conductivity of the sub-surface, both laterally and with depth. Included in these techniques are natural-field methods (magnetotelluric and audiomagnetotellurics) and controlled-source induction methods in both the frequency and time domain. EM methods are more sensitive to conductive (low-resistivity) structures compared to direct current (DC) techniques. This advantage, together with the ability of the magnetotelluric technique to probe several tens of kilometres into the sub-surface, has made these methods very useful in developing a resistivity model for Olkaria geothermal field and also in defining possible geothermal regimes in Olkaria Domes, Longonot and Menengai geothermal prospects that are currently targeted for development.

The Menengai prospect is used as an example in this report. The Menengai geothermal system as defined by resistivity structures seems to exceed 150 km<sup>2</sup> at 1300 m a.s.l. A low-resistivity cap underlain by a high-resistivity core delineates the geothermal system, showing boundaries in all directions except northwest. MT resistivity cross-sections show low resistivity at deeper levels that could be related to heat sources. To define the field better more TEM and MT soundings need to be done west and north of the prospect.

### 1. INTRODUCTION

Geophysical methods, particularly electrical, have proven to be powerful tools in geothermal exploration for decades. Their preference is a result of the direct relationship of resistivity to parameters that characterize geothermal systems. These important parameters are permeability, porosity, salinity, temperature and hydrothermal alteration.

Electromagnetic (EM) methods are used to determine the electrical conductivity of the sub-surface, including natural-field methods (magnetotelluric and audiomagnetotellurics) and controlled-source induction methods. EM methods are more sensitive to low-resistivity structures compared to direct

current (DC) methods. In this report, the factors affecting electrical conductivity of rocks are discussed and the central-loop TEM method and the magnetotelluric (MT) method are introduced. A survey from the Menengai geothermal project in Kenya is used to illustrate the strength of the methods.

## 2. FACTORS AFFECTING ELECTRICAL RESISTIVITY OF WATER-BEARING ROCKS

The electrical resistant property of a material is expressed in terms of its resistivity. If the resistance between opposite faces of a conduction body, that has the length  $l$  and the uniform cross-sectional area  $A$ , is  $R$ , the resistivity,  $\rho$ , of the material is expressed as:

$$\rho = \frac{RA}{l} \quad (1)$$

where  $\rho$  = Resistivity ( $\Omega\text{m}$ );  
 $R$  = Resistance ( $\Omega$ );  
 $A$  = Area ( $\text{m}^2$ ); and  
 $l$  = Length (m).

The electrical conduction in most rocks is essentially electrolytic due to secondary minerals. This is because most mineral grains are insulators, thus the rock matrix itself is an insulator and electric conduction occurs through an aqueous solution of common salts distributed throughout the pores of rocks and alteration minerals at the rock-water interface. The electrical resistivity of rocks depends mainly on the following parameters:

- Porosity and permeability of the rock
- Amount of water (saturation)
- Salinity of the water
- Temperature
- Water-rock interaction and alteration
- Pressure.

### 2.1 Porosity and permeability

Porosity  $\varphi$  is defined as the ratio of void space to the total volume of a material. This is given by the formula:

$$\varphi = \frac{V_\varphi}{V} \quad (2)$$

where  $\varphi$  = Fractional porosity;  
 $V_\varphi$  = Volume of voids ( $\text{m}^3$ ); and  
 $V$  = Total volume of the material ( $\text{m}^3$ ).

Fluid is often important for electrical conduction of a rock, therefore the degree of saturation (dictated by porosity) is of importance to the bulk resistivity of the rock. The following equations usually referred to as Archie's law, describe how resistivity depends on porosity if ionic conduction dominates other conduction mechanisms in a rock (Archie, 1942; Hersir and Björnsson, 1991). Equation 3 is valid if the resistivity of the pore fluid is  $\leq 2 \Omega\text{m}$ ,

$$\rho = \rho_w a \varphi_t^{-n} \quad (3)$$

where  $\rho$  = Bulk resistivity ( $\Omega\text{m}$ );  
 $\rho_w$  = Resistivity of the pore fluid ( $\Omega\text{m}$ );  
 $\phi_t$  = Porosity in proportion of total volume;  
 $\alpha$  = Empirical parameter for describing type of porosity varying from less than 1 for inter-granular porosity to more than 1 for joint porosity, but is usually around 1;  
 $n$  = Cementation factor, usually around 2.

Archie's law is sometimes written as:

$$\rho = \rho_w F \quad ; \quad F = \frac{\rho}{\rho_w} \quad (4)$$

where  $F$  = Formation factor.

The permeability of a rock is the ability of fluids to move within its matrix. Permeability depends on the interconnectivity of the pore spaces within the rock matrix rather than the porosity of the rock. The amount of fluid flowing through a rock can also largely be dictated by fractures (secondary porosity), common in geothermal areas. The wider the fracture, the higher fracture porosity, hence, high permeability is expressed by the following equation (ISL, Michigan State University, 1999):

$$K = \frac{Q\eta L}{AP} \quad (5)$$

where  $K$  = Permeability ( $\text{m}^2$ );  
 $Q$  = Fluid flow rate ( $\text{m}^3/\text{s}$ );  
 $\eta$  = Fluid viscosity ( $\text{kg}/\text{ms}$ );  
 $L$  = Length of the rock (m);  
 $A$  = Cross-sectional area available for flow ( $\text{m}^2$ ); and  
 $P$  = Pressure drop (Pa).

Due to the negligible electrical conduction in most minerals, the majority of charge transport in rocks and sediments occurs in the electrolytes. High mobility (due to high permeability) of the charge carrier within a rock matrix has the effect of lowering the electrical resistivity of the rock.

Geological processes such as faulting, shearing, columnar jointing and weathering usually increase permeability and porosity, therefore increasing electrical conductivity, whereas precipitation of calcium carbonate or silica reduces porosity and hence increases resistivity.

## 2.2 Salinity

An increase in the amount of dissolved ions in the pore fluid can increase the conductivity greatly (Figure 1). Conduction in solutions is largely a function of salinity and the mobility of the ions present in the solution. This is expressed in the equation (Hersir and Björnsson, 1991):

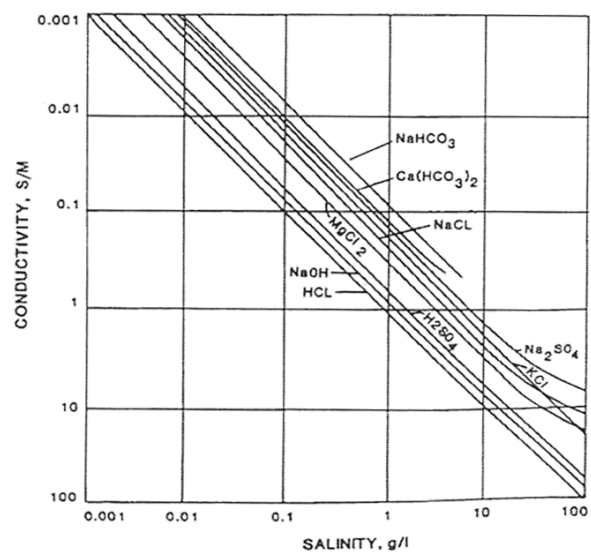


FIGURE 1: Pore fluid conductivity vs. salinity (concentration) for a variety of electrolytes (modif. from Keller and Frischknecht, 1966)

$$\sigma = F(c_1 q_1 m_1 + c_2 q_2 m_2 + \dots) \quad (6)$$

where  $\sigma$  = Conductivity (S/m);  
 $F$  = Faraday's number ( $9.65 \times 10^4$  C);  
 $c$  = Concentration of ions;  
 $q$  = Valence of ions;  
 $m$  = Mobility of ions.

Both an increase in the water content and the total amount of dissolved ions are sometimes associated with geothermal activity.

### 2.3 Temperature

At temperatures well below the critical temperature ( $374^\circ\text{C}$ ), increased temperature enhances the conductivity in the pore fluid (given that the pressure is sufficiently high to prevent boiling). Increase in temperature reduces water viscosity, resulting in increased mobility of ions (Hersir and Björnsson, 1991). This relationship is described by Dakhnov (1962) as:

$$\rho_w = \frac{\rho_{w0}}{1 + \alpha(T - T_0)} \quad (7)$$

where  $\rho_{w0}$  = Resistivity ( $\Omega\text{m}$ ) of the fluid at temperature  $T_0$ ;  
 $\alpha$  = Temperature coefficient of resistivity,  $\alpha \approx 0.023^\circ\text{C}^{-1}$  for  $T_0 = 23^\circ\text{C}$  and  $0.025^\circ\text{C}^{-1}$  for  $T_0 = 0^\circ\text{C}$

Conductivity enhancement, with an increase in temperature, is quite great between 20 and  $350^\circ\text{C}$  for most electrolytes (Figure 2). At higher temperatures, there is a decrease in the dielectric permittivity of water, resulting in a decrease in the number of dissociated ions in solution. This effectively increases fluid resistivity.

### 2.4 Pressure

Confining pressure has the net effect of increasing the bulk resistivity of a rock by decreasing pore volume as the rock is compressed. The pressure effect can be dramatic in fractured rock where the fractures normal to the principle stress close while others remain open. This can cause a significant anisotropy of the rock (Morris and Becker, 2001).

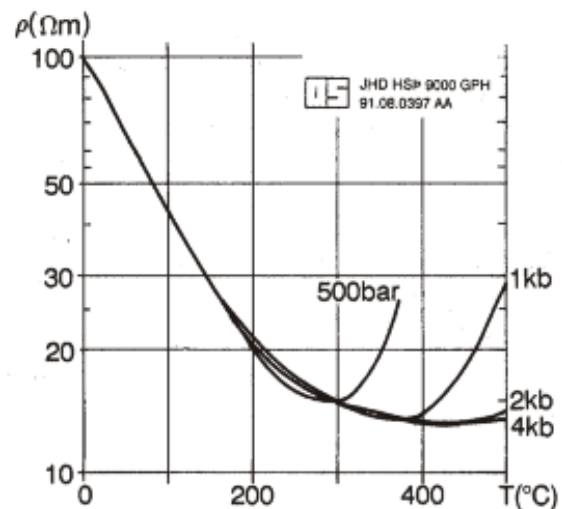


FIGURE 2: Resistivity of an electrolyte as a function of temperature at different pressures (mod. from Quist and Marshall, 1968)

### 2.5 Water-rock interaction and interface conditions

Apart from the reduction in resistivity by the pore fluid, the bulk resistivity of the rock is also reduced by the presence of hydrous secondary minerals (such as clays) as a result of fluid-rock interaction. This interface conductivity (alteration) is expressed by the equation:

$$\sigma = \frac{1}{F} \sigma_w + \sigma_s \quad (8)$$

where  $\sigma$  = Bulk conductivity (S/m);  
 $\sigma_w$  = Conductivity of water (S/m);  
 $\sigma_s$  = Interface conductivity (S/m);  
 $F$  = Formation factor of the rock, given by  $\rho/\rho_w$  (from Equation 3).

The interface conductivity,  $\sigma_s$ , is caused by fluid-matrix interaction and depends mostly on the magnitude of the internal surfaces (porosity) and of their nature (surface conditions). The main two reasons for surface conductivity are the presence of clay minerals (alteration) and surface double-layer conduction.

The alteration process and the resulting type of alteration minerals are dependent on the type of primary minerals, chemical composition of the geothermal fluid and temperature. The intensity of the alteration is furthermore dependent on the temperature, time and the texture of the host rocks. Alteration intensity is normally low for temperatures below 50-100°C. At temperatures lower than 220°C, low-temperature zeolites and the clay mineral smectite are formed. Smectite has hydrated and loosely bound cations between the silica plates, making the mineral conductive and with a high cation exchange capacity (Árnason et al., 2000).

In the temperature range from 220 to about 240-250°C, the low-temperature zeolites disappear and the smectite is transformed into chlorite in a transition zone, the so-called mixed-layered clay zone, where smectite and chlorite coexist in a mixture. At about 250°C the smectite disappears and chlorite is the dominant mineral, marking the beginning of the chlorite zone, hence, highly resistivity, since chlorite minerals have cations that are fixed in a crystal lattice, making the mineral resistive. At still higher temperatures, about 260-270°C, epidote becomes abundant in the so-called chlorite-epidote zone and the resistivity becomes even higher.

In a typical geothermal system, one would expect to find a deep anomaly in electrical conductivity associated with thermal excitation of conduction in the massive crystalline rock comprising the basement. At shallower depths in the section, one would expect to find an anomaly in electrical conductivity associated with a reservoir filled with hot geothermal fluids.

### 3. CENTRAL-LOOP TEM METHOD

#### 3.1 Theory

In the Central-Loop Transient Electromagnetic method, a steady current is transmitted in a wire loop, laid on the ground at the area to be examined (Figure 3). This current is allowed to flow for a sufficiently long time to allow turn-on transients in the ground to dissipate. This steady current is then abruptly terminated in a controlled fashion (Figure 4). At the instant of transmitter turn-off, eddy currents reproduce the static magnetic field due to the transmitter loop but then decay rapidly. The decaying primary magnetic field, in accordance with Faraday's law, induces eddy currents immediately below the transmitter loop. As the initial near-surface eddy current decays,

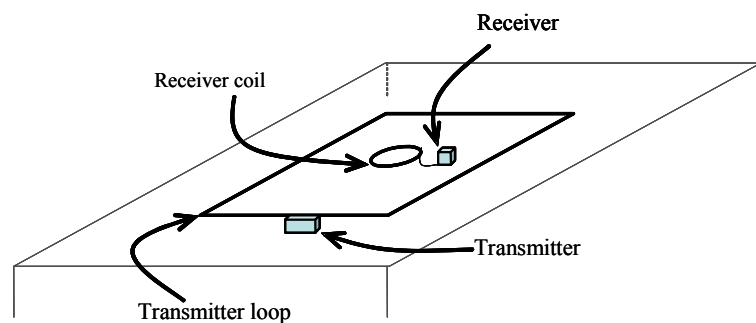


FIGURE 3: Central-loop time domain TEM layout

As the initial near-surface eddy current decays,

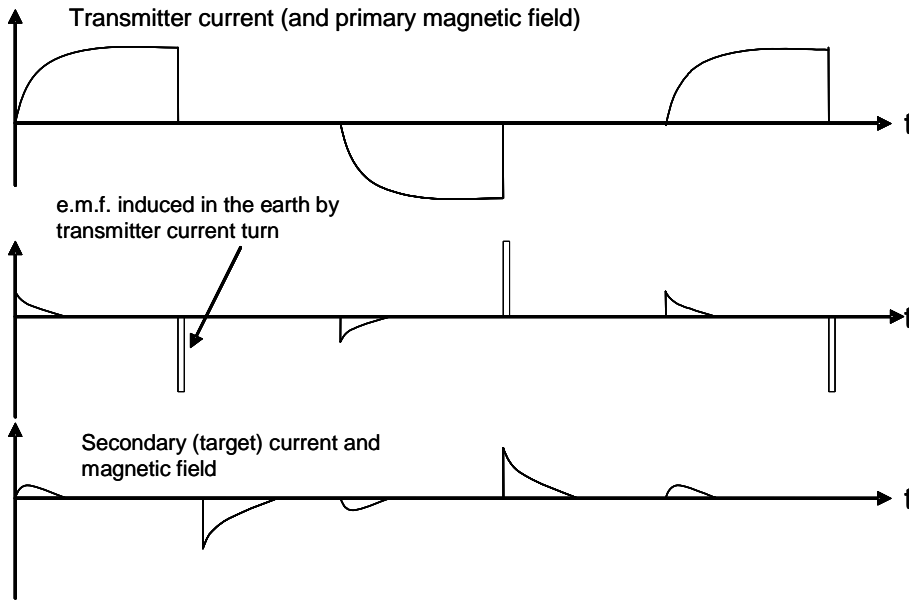


FIGURE 4: Transmitted and received waveforms in a typical time-domain system (after Ward, 1983)

its distribution in the ground in turn induces a secondary magnetic field which also decays with time. This process continues over time with an ever weakening secondary magnetic field inducing currents at increasing depth.

The magnitude and rate of decay of the secondary magnetic field is monitored by measuring the voltage induced in a receiver coil, placed at the centre of the transmitter loop, as a

function of time after the transmitter current is turned off. This is then interpreted in terms of a subsurface resistivity structure (Árnason, 1989).

### 3.2 Confined target responses

For a simple confined conducting target in a resistive half-space, the receiver-coil output voltage is proportional at all times to the time rate-of-change of the secondary magnetic field in the form (Geonics Ltd, 1980):

$$e_0 \propto \frac{I}{\tau} e^{-t/\tau} \tag{9}$$

- where  $\tau$  = L/R, i.e. time-constant of the target;
- $L$  = Inductance of the target (H);
- $R$  = Target resistance ( $\Omega$ ).

From the above expression, we see that conductive targets (i.e. those having small resistance and therefore a large value of  $\tau$ ) yield signals with small amplitude but decay relatively slowly. Resistive targets, however, have high initial amplitudes that decay rapidly.

As an example take a conducting sphere (to represent a confined target, i.e. a conductor surrounded by an insulator) (Figure 5a), with a radius  $r$  and a conductivity  $\sigma$  in a uniform magnetic field  $H_p$  which is suddenly terminated at time  $t = 0$ . Currents will immediately flow on the surface of the sphere (early times) with a distribution that tries to maintain the original uniform magnetic field within the sphere. The current distribution at the early times (Figure 5b) is independent of the conductivity of the sphere. We can say that at this stage we are in the high-frequency limit since the current distribution is similar to that which would flow if the sphere was located in a very high-frequency alternating magnetic field. The electrical skin-depth,  $\delta$ , of the sphere material defined by the following relationship:

$$\delta = \left( \frac{2}{\mu\sigma\omega} \right)^{1/2} \tag{10}$$

where  $\mu = 4\pi \times 10^{-7}$  (H/m);  
 $\omega = 2\pi f$ ;  
 $f =$  Frequency (Hz),

The high frequency in this case is such that the skin-depth is much less than the radius of the sphere.

Figure 5c shows a cross-section cutting an equatorial plane of the conductive sphere; at time  $t = 0$  the current is concentrated at the surface layer of the sphere. However the amplitude of the current commences to decrease due to ohmic losses in the conductive sphere material. The local magnetic field due to the current also decreases inducing electromagnetic field (through Faraday's Law) which causes new current to flow as shown in Figure 5d. This process continues with the result that the current flow moves inward as time elapses. The currents appear to be diffusing radially inwards as a result of the interaction with their magnetic fields in the conductive body. This period, when the current distribution is in motion, is termed as the 'intermediate-times'. During this period the magnetic field associated with the decreasing currents decays rapidly with time.

A stage is reached, however, where the relative spatial current distribution becomes invariant with time but decreases at an equal rate, with the form indicated in

Figure 5e. Near the sphere centre, the current density increases linearly with radial distance becoming relatively uniformly distributed at one-half the radius and slightly decreasing towards the edge. This period is termed as the 'late-times'. The inductance and resistance associated with each current ring have stabilized and from this point onwards, both currents and their associated external magnetic fields commence to decay exponentially with a time-constant given by (Geonics Ltd, 1980) as:

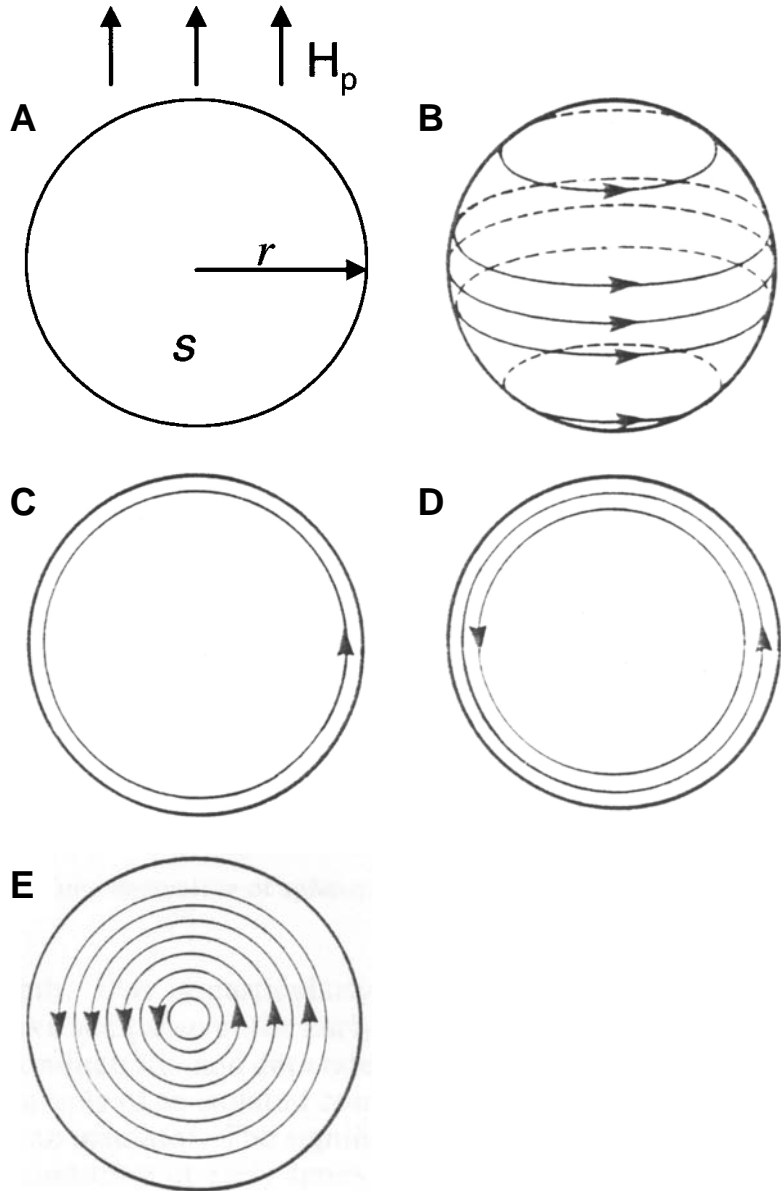


FIGURE 5: Target conductive sphere and current distribution

$$\tau = \frac{\sigma \mu r^2}{\pi^2} \tag{11}$$

For any confined conductor, the current distribution at the early times is a function of time and the overall decay is not exponential. At the late times however, the current distribution becomes invariant with time and the decay becomes exponential at a rate determined by the shape, size and conductivity of the body.

### 3.3 Layered earth response

When dipole moment of a vertical magnetic dipole transmitter located on a homogenous half-space, shown in Figure 6, is abruptly reduced to zero at time  $t_0$ , a short-duration voltage pulse is induced in the ground which causes a loop of current to flow in the immediate vicinity of the transmitter wire (in accord with Faraday's law) distributed in such a manner as to maintain the magnetic field everywhere as it existed before turn-off.

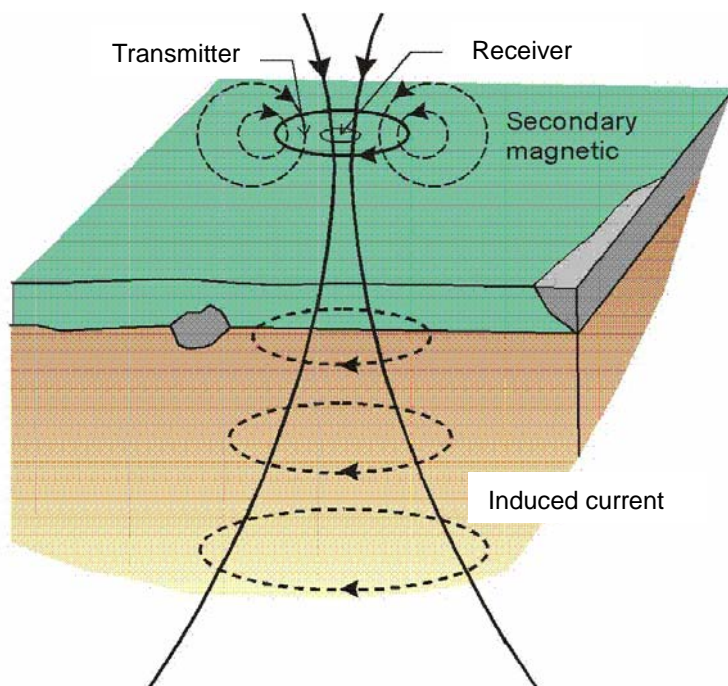


FIGURE 6: Transient current flow in the ground (mod. from Hersir and Björnsson, 1991)

The finite ground resistivity causes the amplitude of this current to start decaying immediately. This surface current flow decreases as  $r^{-4}$  from the transmitter, where  $r$  is distance from the transmitter (Geonics Ltd, 1980). Close to the transmitter the induced surface current starts to diffuse into the homogeneous half-space, whereas the current at a great distance maintains the value dictated by  $r^{-4}$  fall-off. As time elapses, the current effectively appears to move outwards and downwards as a diffusing ring due to the deficiency of current near the transmitter (Figure 6). The magnitude of the current induced at time  $t = 0$  at the surface is independent of the conductivity but its apparent velocity at which its ring expands is inversely proportional to the square root of the conductivity of the medium it is

diffusing through. This decaying current and magnetic flux induces a voltage that causes more current to flow, but now at a larger distance from the transmitter loop, and also at greater depth. This deeper current flow also decays due to finite resistivity of the ground, inducing even deeper current flow and so on.

The amplitude of the current flowing as a function of time is measured by monitoring its decaying magnetic field using a small multi-turn receiver coil located at the centre of the transmitter loop. By taking measurements of the voltage out of the receiver coil at successively later times, measurement is made of the current flow and thus also of the electrical resistivity of the earth at successively greater depths.

Induced voltage in the receiver coil (in the frequency domain), due to alternating current  $I_0 e^{i\omega t}$  transmitted into a circular loop of radius  $r$  on the top of an N-Layered halfspace, is given by (Árnason, 1989):

$$V_c(\omega, r) = A_r n_r A_s n_s I_0 e^{i\omega t} \frac{-i\omega\mu_0}{\pi r} \int_0^\infty \frac{\lambda^2}{m_0} \frac{S_0}{S_0 - T_0} J_1(\lambda r) d\lambda \quad (12)$$

where  $A_r$  = Cross-sectional area of the receiver coil (m<sup>2</sup>);  
 $n_r$  = Number of windings in the receiver coil;  
 $\mu_0$  = Magnetic permeability in vacuum (H/m);  
 $A_s$  = Cross-sectional area of the transmitter loop (m<sup>2</sup>);  
 $n_s$  = Number of windings in the transmitter loop;  
 $r$  = Radius of the source loop (m).

$S_0$  and  $T_0$  are given by the recursion relations;

$$S_{i-1} = S_i \cosh(m_i d_i) - T_i \sinh(m_i d_i)$$

$$T_{i-1} = \frac{m_i}{m_{i-1}} [ S_i \sinh(m_i d_i) - T_i \cosh(m_i d_i) ]$$

$$S_{N-1} = 1; T_{N-1} = \frac{m_N}{m_{N-1}}$$

where  $d_i$  = The thickness of the  $i$ 'th layer (m); and  
 $m_i$  = The impedance of the  $i$ 'th layer.

The quantities  $S_0$  and  $T_0$  which determine the voltage in Equation 12 depend on  $\omega$  and the conductivities,  $\sigma_i$  through  $m = \sqrt{\lambda^2 - k^2}$  where  $k^2 = \omega^2 \mu \epsilon - i\omega\mu\sigma$  ( $\epsilon$  is the dielectric permittivity). In the quasi-stationary approximation  $\epsilon \sim 0$ , hence  $k^2 = -i\omega\mu\sigma$ .

Mutual impedance between the source and the receiver coil (by analogy with Ohm's law) is defined by the ratio between the measured voltage and the transmitted current. From Equation 12, the mutual impedance for central-loop configuration is:

$$Z_c(\omega, r) = \frac{V_L(\omega, r)}{I_0 e^{i\omega t}} = A_r n_r A_s n_s \frac{-i\omega\mu_0}{\pi r} \int_0^\infty \frac{\lambda^2}{m_0} \frac{S_0}{S_0 - T_0} J_1(\lambda r) d\lambda \quad (13)$$

Equation 12 can be expressed in the time domain by a Fourier expansion of the function describing the transmitted current (Arnason, 1989). If the transmitted current is described by the function  $I(t)$ , a Fourier expansion of the current function will be:

$$I(t) = \frac{1}{(2\pi)^{1/2}} \int_{-\infty}^{\infty} \tilde{I}(\omega) e^{i\omega t} d\omega \quad (14)$$

where

$$\tilde{I}(\omega) = \frac{1}{(2\pi)^{1/2}} \int_{-\infty}^{\infty} I(t) e^{-i\omega t} dt \quad (15)$$

From Equation 13, the induced voltage in the receiver coil in terms of mutual impedance (as a function of frequency) and the Fourier transform of the transmitted current are expressed as:

$$V_c(t, r) = \frac{1}{(2\pi)^{1/2}} \int_{-\infty}^{\infty} Z_L(\omega, r) \tilde{I}(\omega) e^{i\omega t} d\omega \quad (16)$$

The measured voltage as a function of time after the steady current is abruptly turned off at  $t = 0$  is then expressed by:

$$V_-(t) = \frac{-I_0}{2\pi} \int_{-\infty}^{\infty} \frac{Z(\omega)}{i\omega} e^{i\omega t} d\omega = \frac{I_0}{2\pi} \int_{-\infty}^{\infty} \Phi(\omega) e^{i\omega t} d\omega \quad (17)$$

If for simplicity, we define:

$$\Phi(\omega) = \frac{Z(\omega)}{-i\omega} \quad (18)$$

$\Phi(\omega)$  only depends on  $\omega$  through  $\omega^2$  and  $i\omega$ , hence:

$$\Phi^*(-\omega) = \Phi(\omega) \quad (19)$$

where \* denotes the complex conjugation and therefore

$$\text{Re } \Phi(-\omega) = \text{Re } \Phi(\omega) ; \text{Im } \Phi(-\omega) = -\text{Im } \Phi(\omega) \quad (20)$$

Equation 17 can therefore be simplified to:

$$V_-(t) = \frac{2I_0}{\pi} \int_{-\infty}^{\infty} \text{Re } \Phi(\omega) \cos(\omega t) d\omega \quad (21)$$

Transient voltage generated in the receiver coil due to a linearly ramped step function is given by (Árnason, 1989):

$$V(t) = \frac{I_0}{TOFF} \int_{-TOFF}^0 V_-(t-\tau) d\tau = \frac{I_0}{TOFF} \int_t^{0+TOFF} V_-(\tau) d\tau \quad (22)$$

In practice the current is not abruptly turned off, but turned off linearly in a time interval of length TOFF.

For a homogeneous half-space of conductivity  $\sigma$ , the induced voltage in the receiving coil is given approximately by (Árnason 1989):

$$V(t, r) = I_0 \frac{C(\mu_0 \sigma r^2)^{2/3}}{10\pi^{1/2} t^{5/2}}, \text{ where } C = A_r n_r A_s n_s \frac{\mu_0}{2\pi r^3} \quad (23)$$

As was discussed in Section 3.2, the time-behaviour of the diffusing current is in three phases; early times, intermediate and late times (Figure 7). At late times the measured voltage  $V(t)$  decays in time as  $t^{-5/2}$  and varies as  $\sigma^{3/2}$  (Árnason 1989), thus making TEM intrinsically more sensitive to small variations in the conductivity than conventional resistivity methods.

Apparent resistivity  $\rho_a$ , of a homogeneous half-space in terms of induced voltage at late times after the source current is turned off is given by (Árnason 1989):

$$\rho_a = \frac{\mu_0}{4\pi} \left[ \frac{2\mu_0 A_r n_r A_s n_s I_0}{5t^{5/2} V(t,r)} \right]^{2/3} \tag{24}$$

- where  $t$  = Time elapsed after the transmitter current is turned off (s);
- $A_r$  = Cross-sectional area of the receiver coil (m<sup>2</sup>);
- $n_r$  = Number of windings in the receiver coil;
- $\mu_0$  = Magnetic permeability in vacuum (H/m);
- $A_s$  = Cross-sectional area of the transmitter loop (m<sup>2</sup>);
- $n_s$  = Number of windings in the transmitter loop;
- $I_0$  = Transmitter current (A);
- $V_{(t,r)}$  = Measured voltage (V).

In the case of a homogeneous half-space of resistivity  $\rho$ , the apparent resistivity gives the true resistivity at late times.

The definition of apparent resistivity is based on the time behaviour of the receiver coil output voltage at late times when it decays as  $t^{-5/2}$  as seen from Figure 7. At earlier and intermediate times, receiver voltage is too low (relative to the dashed line indicating the approximation of late-time voltage back in time) and thus, from Equation 24, the apparent resistivity  $\rho_a(t)$  will be too high. This results in a "descending branch" at early time where the apparent resistivity is higher than the half-space resistivity as shown in Figure 8. However, at late time, the apparent resistivity  $\rho_a(t)$  is equal to half-space resistivity  $\rho_1$ .

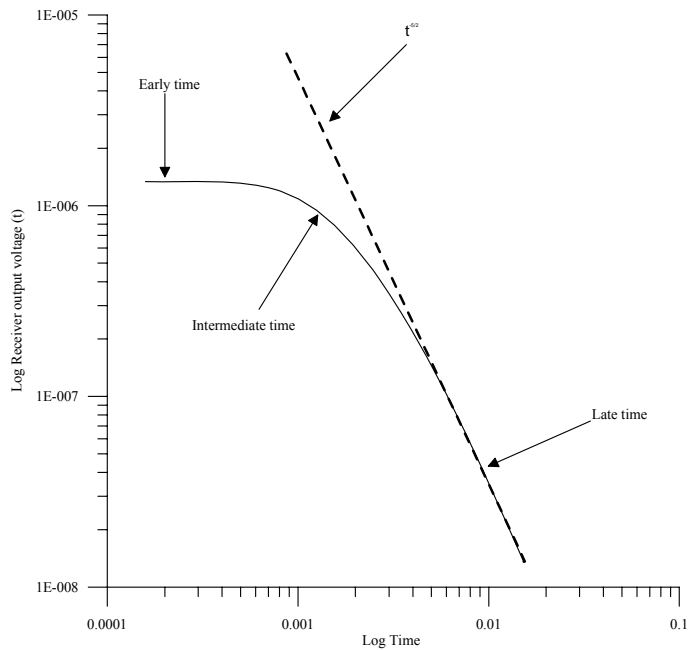


FIGURE 7: Log plot of receiver output voltage versus time

If we let the earth be two-layered with the upper layer having resistivity  $\rho_1$ , and thickness  $h$ , and basement resistivity  $\rho_2$  ( $>\rho_1$ ), at early times when the currents are entirely in the upper layer of resistivity  $\rho_1$  the decay curve will look like that of a homogeneous half-space of resistivity  $\rho_1$  if the layer is sufficiently thick (Figure 7), and the apparent resistivity curve will look like Figure 8 for a while. Later on the currents will lie in both layers, and at much later times, they will be located entirely in the basement of resistivity  $\rho_2$ .

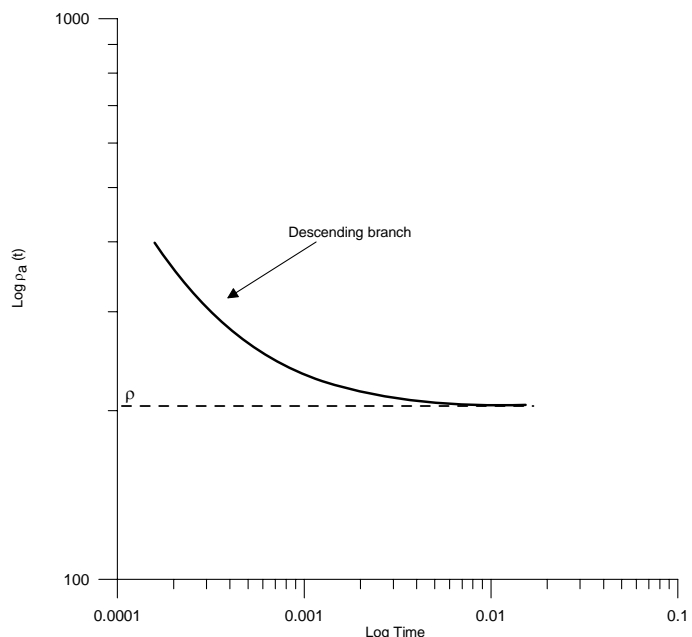


FIGURE 8: Apparent resistivity of a half-space versus time

Since  $\rho_2 > \rho_1$ , Equation 23 shows that (as indicated in curve a in Figure 9) the measured voltage will now be less than it would have been for the homogeneous half-space of resistivity  $\rho_1$ . The effect on

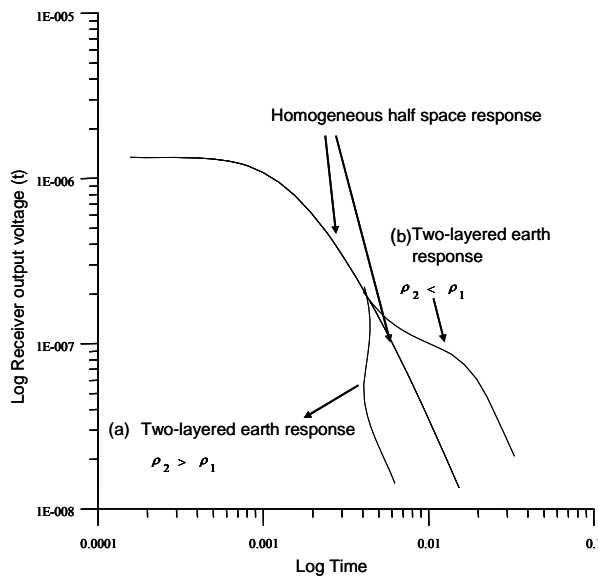


FIGURE 9: Time domain electromagnetic (TDEM) receiver output voltage, two layered earth

the apparent resistivity curve is shown in Figure 10a. At late times, all the currents are in the basement; therefore, the apparent resistivity  $\rho_a(t)$  becomes equal to  $\rho_2$ .

In a scenario where  $\rho_2 < \rho_1$ , late times voltage response will be greater than that from a homogeneous half-space of resistivity  $\rho_1$  (as shown in curve b in Figure 9), and the apparent resistivity curve correspondingly becomes that of Figure 10b, becoming equal to the new value of  $\rho_2$  at late times. Because of a relatively conductive basement, there is a region of intermediate times (shown on Figure 10b at  $t^*$ ), where the voltage response temporarily falls before continuing on to adopt the value appropriate to  $\rho_2$ . This appears as an overshoot in the apparent resistivity curve when changing from the resistive upper layer ( $\rho_1$ ) to a more conductive basement.

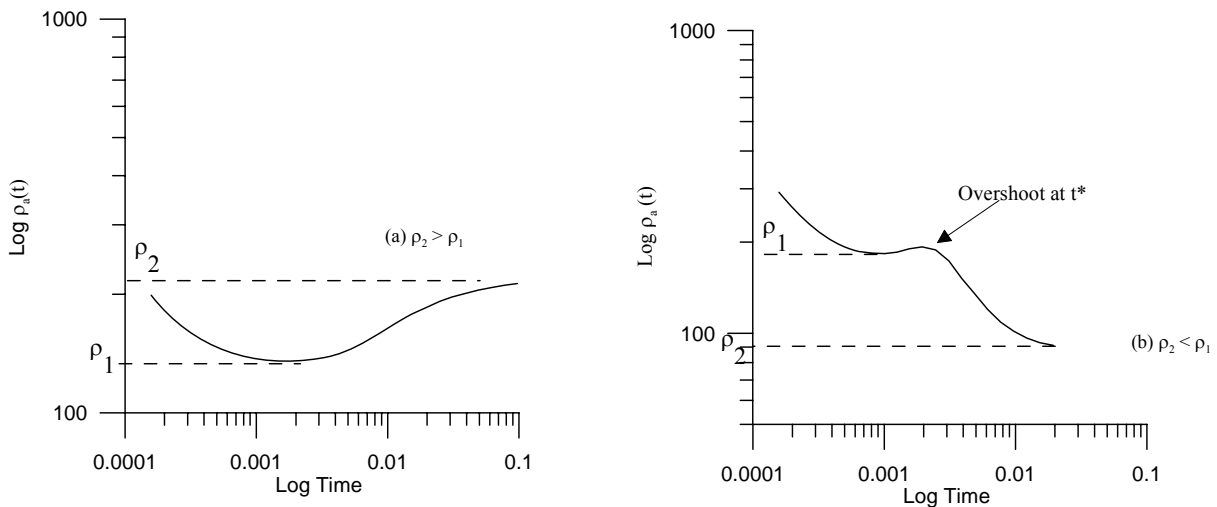


FIGURE 10: TDEM - apparent resistivity, two layered earth, a)  $\rho_2 > \rho_1$ ; b)  $\rho_2 < \rho_1$

#### 4. MAGNETOTELLURIC METHOD

##### 4.1 Theory

The Magnetotelluric (MT) method is a passive surface geophysical technique which uses the time varying earth's natural electric and magnetic fields to study electrical resistivity of the subsurface. Magnetic and electrical fields are measured in the frequency band  $10^{-4}$  to 10 kHz, with high frequencies ( $>1$  Hz) coming from thunderstorm activities in the equatorial belt while low frequencies ( $<1$  Hz) occur due to the interaction between the solar wind and the earth's magnetic field (magnetosphere) and ionosphere.

Natural electric and magnetic field strengths are simultaneously recorded in two orthogonal, horizontal directions as a function of time. The resulting time-series data is then Fourier transformed to the frequency domain and processed to derive the impedance tensors of the apparent resistivities and phase.

For geothermal exploration, the MT method targets deep brine reservoirs and hot (or partially molten) rocks that act as the heat source for a geothermal system under survey (Ward and Wannamaker, 1983).

## 4.2 Homogeneous earth

When electromagnetic monochromatic plane waves propagate downwards (along the z-axis) in a homogeneous and isotropic medium, the electric and magnetic field vectors are orthogonal and the ratio of the electric to magnetic field intensity is a characteristic measure of the electromagnetic properties of the medium, often called characteristic impedance (Cagniard, 1953; Keller and Frischknecht, 1966). This characteristic impedance is described by the following equation:

$$Z = \frac{\omega\mu_0}{k} = \frac{E_x}{H_y} = -\frac{E_y}{H_x} \quad (25)$$

where  $Z$  = Characteristic impedance;  
 $\omega$  = Angular frequency ( $2\pi f$ ) where  $f$  is frequency (Hz);  
 $\mu_0$  = Magnetic permeability (H/m);  
 $E_{x,y}$  = Electric field intensity (V/m) in x,y direction;  
 $H_{x,y}$  = Magnetic field intensity (T or Tesla) in x,y;  
 $k$  =  $\sqrt{i\omega\mu(i\omega\varepsilon + \sigma)}$  stands for the wave propagation constant;  
 $\varepsilon$  = Dielectric permittivity (C/Vm);

If displacement currents are neglected,  $k = \sqrt{i\omega\mu\sigma}$  and Equation 25 can be rewritten as:

$$Z = \frac{\omega\mu_0}{\sqrt{\rho i\mu_0\sigma\omega}} = \sqrt{i}\sqrt{\omega\mu_0\rho} = \sqrt{\omega\mu_0\rho}e^{i\pi/4} \quad (26)$$

and there is a  $\pi/4 = 45^\circ$  phase difference between  $E_x$  and  $H_y$ , with  $E_x$  leading  $H_y$ . (Figure 11).

The resistivity of the homogeneous half-space is given as (Ward and Wannamaker, 1983):

$$\rho = \frac{1}{\omega\mu_0}|Z|^2; \quad Z = \frac{E_x}{H_y} \quad (27)$$

This can be reformulated by using the magnetic field intensity,  $H_z$ , and the magnetic field as related by  $\vec{B} = \mu\vec{H}$  ( $\mu = 4\pi \times 10^{-7}$ ). In practice the electric field is expressed in mV/km and the magnetic field in nT (or  $10^{-9}$  Tesla = gamma). Therefore, Equation 27 can be expressed as:

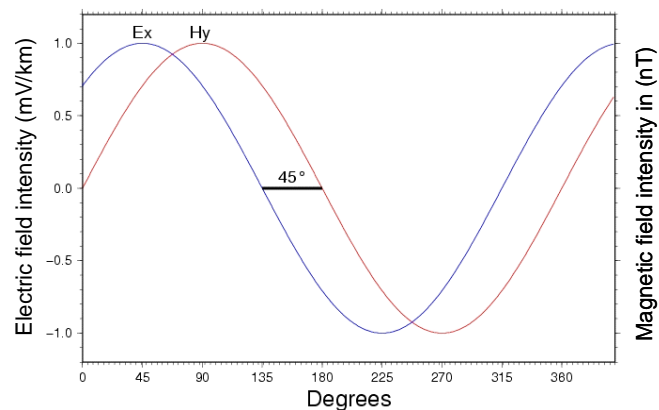


FIGURE 11: Homogeneous half-space response of electric and magnetic field intensity

$$\rho = \frac{T}{2\pi\mu} \left| \frac{E_x 10^{-6} \mu}{B 10^{-9}} \right|^2 = \frac{T\mu}{2\pi} \left| \frac{E_x}{B_y} \right| 10^6 = 0.2T \left| \frac{E_x}{B_y} \right|^2 \quad (28)$$

where  $T$  = Period in seconds;  
 $\rho$  = Resistivity ( $\Omega\text{m}$ ).

For a non-homogeneous earth, apparent resistivity,  $\rho_a$ , and phase,  $\theta_a$ , are defined as:

$$\rho_a = 0.2T|Z_0|^2 \quad \text{and} \quad \theta_a = \arg(Z_0) \neq 45^\circ$$

where  $Z_0$  = Impedance at the surface

### 4.3 Layered earth

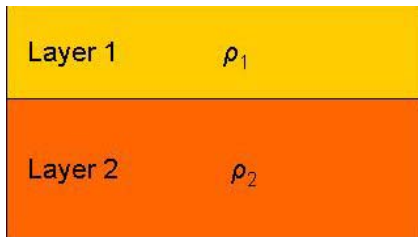
For horizontally N-layered earth the plane wave impedance is given by the recursive formula (Ward and Wannamaker, 1983):

$$\hat{Z}_N = Z_N = \frac{\omega\mu}{k_N} \quad \hat{Z}_{n-1} = Z_{n-1} \frac{\hat{Z}_n + Z_{n-1} \tanh(ik_{n-1}h_{n-1})}{Z_{n-1} + \hat{Z}_n \tanh(ik_{n-1}h_{n-1})} \quad (29)$$

where  $Z_n = \frac{\mu_0\omega}{k_n}$  (intrinsic impedance of the  $n^{\text{th}}$  layer); with

$k_n$  =  $\sqrt{(i\omega\mu\sigma_n)}$ ; and  
 $h_n$  = Thickness of the  $n^{\text{th}}$  layer;

$\hat{Z}_n$  = Impedance at the top of the  $n^{\text{th}}$  layer and  $Z_1 = Z_0$  is that on the surface.



For two-layered earth (Figure 12), Equation 28 becomes:

$$\hat{Z}_1 = Z_1 \frac{\hat{Z}_2 + Z_1 \tanh(k_1 h_1)}{Z_1 + \hat{Z}_2 \tanh(k_1 h_1)} \quad (30)$$

where  $Z_1 = Z_0$  = Impedance at the surface; and

FIGURE 12: Two-layered earth

$$k_1 = \sqrt{\frac{i\omega\mu}{\rho_1}} = \sqrt{\frac{i2\pi\mu}{\rho_1 T}}$$

For a large period  $T$ ,  $k_1 h \ll 1$ , and therefore,  $\tanh(ik_1 h_1) \approx ik_1 h_1$ . Equation 30 can, in this case, be rewritten as:

$$Z_0 = Z_1 \frac{\hat{Z}_2 + iZ_1 k_1 h_1}{Z_1 + i\hat{Z}_2 k_1 h_1} = Z_1 \frac{Z_2 + iZ_1 k_1 h_1}{Z_1 + iZ_2 k_1 h_1} \quad (31)$$

When  $\rho_1 \gg \rho_2$ , i.e. we have a good conductor at depth  $h_1$  and  $Z_1 \gg \hat{Z}_2$ , Equation 31 becomes:

$$Z_0 = Z_1 \frac{Z_2 + iZ_1 k_1 h_1}{Z_1 + Z_2 k_1 h_1} \approx iZ_1 k_1 h_1 = \frac{i\omega\mu}{k_1} * k_1 h_1 = i\omega\mu h_1 \quad (32)$$

and

$$\rho_a = \frac{1}{\omega\mu} |Z_0|^2 = \frac{1}{\omega\mu} (\omega\mu h_1)^2 = \frac{2\pi\mu h_1^2}{T} \quad (33)$$

The depth to the good conductor,  $h_1$ , can be calculated from  $\rho_a$  at large  $T$  according to:

$$h_1 = \sqrt{\frac{\rho_a T}{2\pi\mu}} \quad (34)$$

Equation 33 shows that when plotting  $\log \rho$  vs.  $\log T$  the slope is -1 at large  $T$

When  $\rho_1 \ll \rho_2$  and  $Z_1 \ll Z_2$ , i.e. we have an insulator at depth  $h_1$ , then from Equation 31:

$$Z_0 = Z_1 \frac{Z_2 + iZ_1 k_1 h_1}{Z_1 + iZ_2 k_1 h_1} \approx Z_1 \frac{1}{ik_1 h_1} = \frac{\omega\mu}{ik_1^2} \frac{1}{h_1} = \frac{1}{\sigma_1 h_1} = \frac{1}{S} \quad (35)$$

where  $S$  = The conductance of layer 1; and

$$\rho_a = \frac{1}{\omega\mu} |Z_0|^2 = \frac{1}{\omega\mu} \frac{1}{S^2} = \frac{T}{2\pi\mu} \frac{1}{S^2}$$

Thus, we can calculate the conductance of layer 1 from  $\rho_a$  at large  $T$  according to

$$S = \sqrt{\frac{T}{2\pi\mu\rho_a}}$$

The amplitude of the electromagnetic wave decreases due to Ohmic loss, as it propagates in the earth. A characteristic depth of penetration, skin depth  $\delta$  (m), is defined as the depth where the electromagnetic field amplitude has decayed by  $e^{-1}$  with respect to its value at the surface.

$$\delta = \frac{1}{\text{Im}k} = \frac{1}{\text{Im}\sqrt{i\omega\mu\sigma}} = \sqrt{\frac{2}{\omega\mu\sigma}} = \sqrt{\frac{2T\rho}{2\pi \times 4\pi \times 10^{-7}}} = \frac{10^3}{\pi} \sqrt{\frac{20}{8}} \sqrt{\rho T}$$

$$\delta \approx 500\sqrt{T\rho}, \text{ where } T \text{ is in s and } \rho \text{ in } \Omega\text{m} \quad (36)$$

#### 4.4 Static shifts

The presence of near surface resistivity inhomogeneities can distort the electrical field, since the field is not continuous across a resistivity boundary. This galvanic distortion effect is known as static shift. This effect shifts the MT apparent resistivity sounding curve (i.e.  $\log\rho_a$  vs.  $\log T$ ) by some constant scale factor. Static shift does not affect the phases of the MT impedance tensor.

Since a magnetic field is relatively unaffected by surface inhomogeneities, controlled-source magnetic-field sounding such as Central-loop Transient Electromagnetic (TEM) sounding can be used to correct for static shifts. The MT sounding curve is shifted vertically so that the high-frequency part of the MT curve agrees with the TEM curve. The low-frequency MT curves then provide an undistorted picture of the deep resistivity section (Jones, 1988).

**5. TEM AND MT RESISTIVITY SURVEY IN MENENGAI**

**5.1 Geological setting**

The Kenya Rift Valley is a prominent feature that is of great geographic and geological interest. It is a part of the East Africa Rift system, an intra-continental divergent zone where rift tectonics are accompanied by active volcanism. Several Quaternary volcanoes are found within the Kenya segment of the rift floor. Some of these volcanic centres are dotted with hydrothermal activities and are pictured to host geothermal systems driven by magmatic heat sources (Mungania, 2004). Menengai geothermal prospect is located within an area characterized by complex tectonic activity associated with a rift triple junction. This is at the zone where the Nyanza rift joins the main Kenya rift (Figure 13).

Menengai is located about 20 km south of the equator. The major structural systems in the area are the Menengai caldera, the Molo tectonic axis and the Solai graben (Figure 14). Menengai caldera is elliptical with the major and minor axis measuring about 12 and 8 km, respectively. The ring structure has been disturbed by the Solai graben faults on the northeast end and one fracture at the south-southwest end of the caldera wall extending southwards (Figure 14). The Molo TVA / Ol rongai fracture system intersects the Menengai caldera on the north-northwest part. The caldera floor covers an area of about 88 km<sup>2</sup>, and is partially covered by young rugged lava flows that are post caldera in age. Most of the lavas are from fissure eruptions that flowed out of fracture openings. An extensive area around the caldera is to a large extent covered by pyroclastics erupted from centres that are associated with Menengai volcano.

The Molo TVA is quite a prominent structural feature represented on the surface by a zone with a concentration of faults and fractures along which volcanic eruptions have taken place (Figure 14). The other structure that is of significance in this area is the Solai tectonic axis. It comprise numerous faults/fracture systems trending N-S. It cuts through the caldera from the northern end and extends southwards beneath the Menengai volcanic pile. This fracture system is important as a hydrological control and possibly contributes to permeability enhancement of the brittle lava formations underlying the Menengai eruptives.

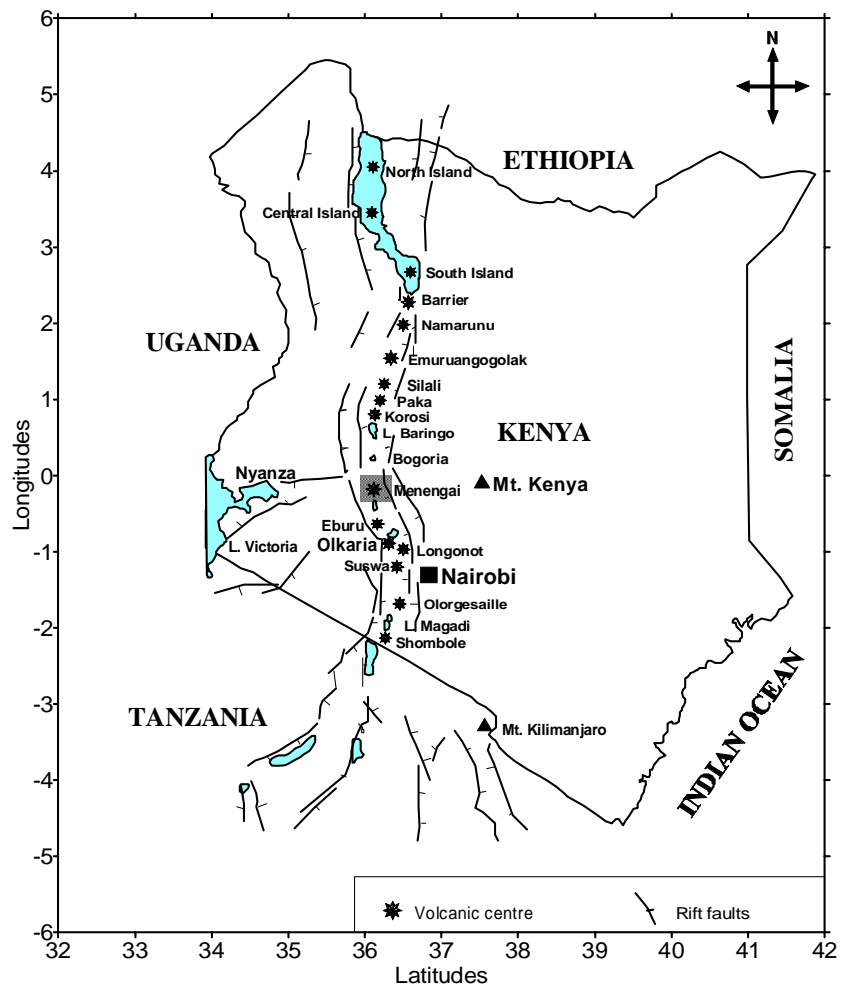


FIGURE 13: Map of Kenya showing location of Menengai geothermal prospect and other Quaternary volcanic systems along the Kenyan rift axis

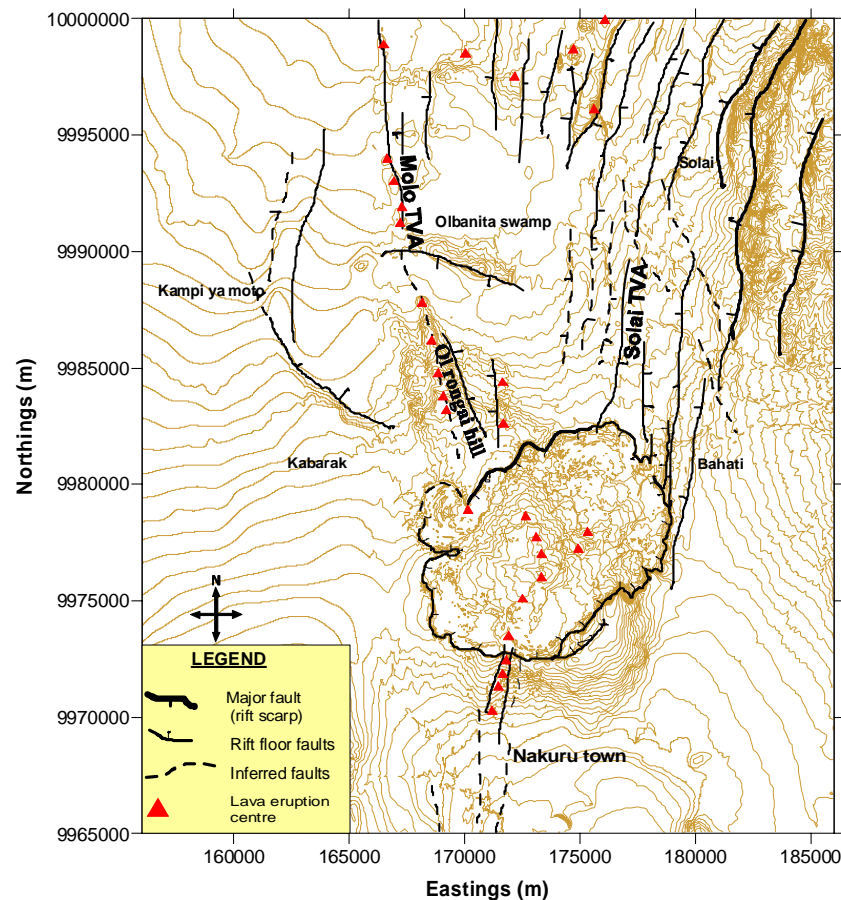


FIGURE 14: Map of Menengai geothermal prospect showing the caldera outline, volcanic centres and other main structures

## 5.2 TEM survey

A total of 62 TEM soundings, covering an area of about 50 km<sup>2</sup>, were carried out in the Menengai prospect area using a central loop TEM array. About 38 soundings were done within the caldera floor and its surroundings, while the remaining soundings were scattered in other parts of the prospect field (Figure 15).

The equipment that was used for this survey (purchased from Zonge Engineering Co. except for the power generator) comprised the following units:

- Transmitter - GGT-3 (maximum loop current of 12 amps)
- Transmitter controller - XMT-16
- Data logger - GDP-16 (three channel unit)
- Receiver coil - TEM/3 (receiver moment of 10000 m<sup>2</sup>)
- Voltage regulator - VR-1
- Power source - 5HP Honda generator (120 Vac at 400Hz)

In all the soundings, a 300 m x 300 m transmitter wire loop was used. A half-duty square wave current was transmitted at frequencies 16, 8, 4 and 2 Hz. Logarithmically spaced sampling gates were used with 16 Hz having 25 gates starting at 36.14  $\mu$ s to 12.18 ms; 4 Hz had 31 sampling gates starting at 36.14  $\mu$ s to 48.42 ms and 2 Hz had 34 gates starting at 84.18  $\mu$ s to 96.85 ms. At each repetition rate, several repeated transients were stacked and stored in a memory cache inside the data logger and were later transferred to a personal computer (PC) for processing.

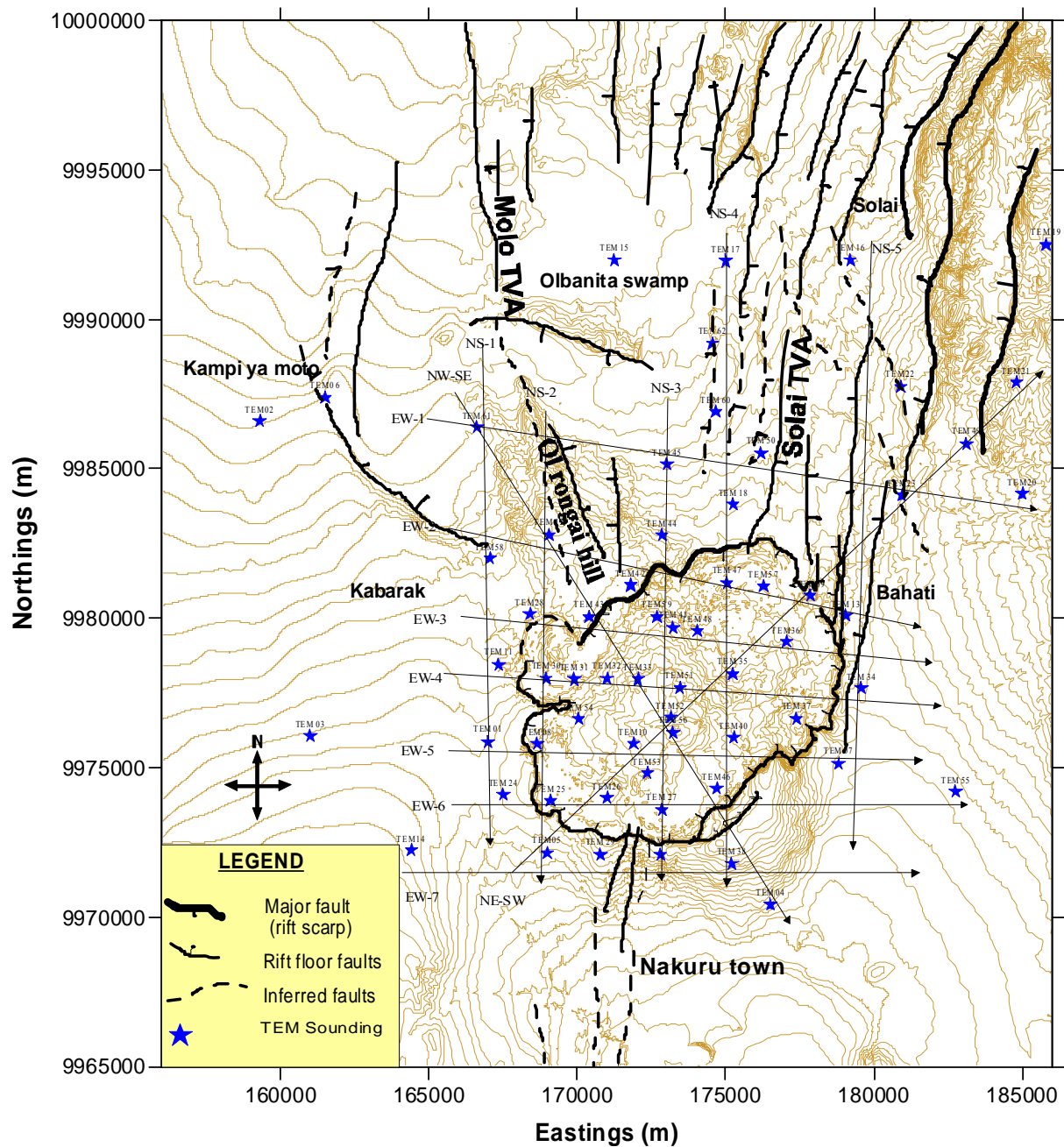


FIGURE 15: Map showing location of TEM soundings and resistivity cross-sections

The transmitter and the receiver timing were controlled by synchronized high-precision crystal clocks. This was achieved by synchronizing the receiver and the transmitter controller prior to the data acquisition procedure to ensure that induced voltage was measured by the receiver only after the transmitter was turned off.

### 5.2.1 Data processing and interpretation

TEMX program was used to read raw data files downloaded from the GDP-16 receiver. This program calculates averages and standard deviations of repeated transient voltage measurements and calculates late time apparent resistivity as a function of time. The program has a graphical-user interface (GUI) and offers the possibility of editing raw data by rejecting some of the noisy readings.

The CLTINV interpretation program was used to perform 1D inversion on the data. The program was developed by Knútur Árnason at ÍSOR. The program assumes that the source loop is a square loop

and that the receiver coil/loop is at the centre of the source loop. The current wave form is assumed to be a half-duty bipolar semi-square wave with exponential current turn-on and linear current turn-off.

The inversion algorithm used in the program is the nonlinear least-squares inversion of the Levenberg-Marquardt type (Árnason, 1989). The misfit function is the root-mean-square difference between measured and calculated values (chisq), weighted by the standard deviation of the measured values. The user is offered the option of choosing whether the program fits the measured voltage or the late time resistivity values. Smooth models were also achieved by using Occam's (minimum structure) inversion. In this case many layers (20) were used with fixed equal thicknesses on a log-scale between the surface and the basement depth and variable resistivity values. The variation in resistivity was kept smooth with little contrast between layers (Appendix I).

### 5.3 MT survey

In all, 67 MT soundings were carried out in Menengai prospect. The sounding distribution over the prospect area is as shown in Figure 16. For the MT soundings 3 sets of 5-channel MT data acquisition systems were used (MUT-5A) from Phoenix Geophysics-Canada, as shown in Figure 17. MT-5A systems acquire MT data in frequencies ranging from about 400 Hz to 0.0000129 Hz (a period of

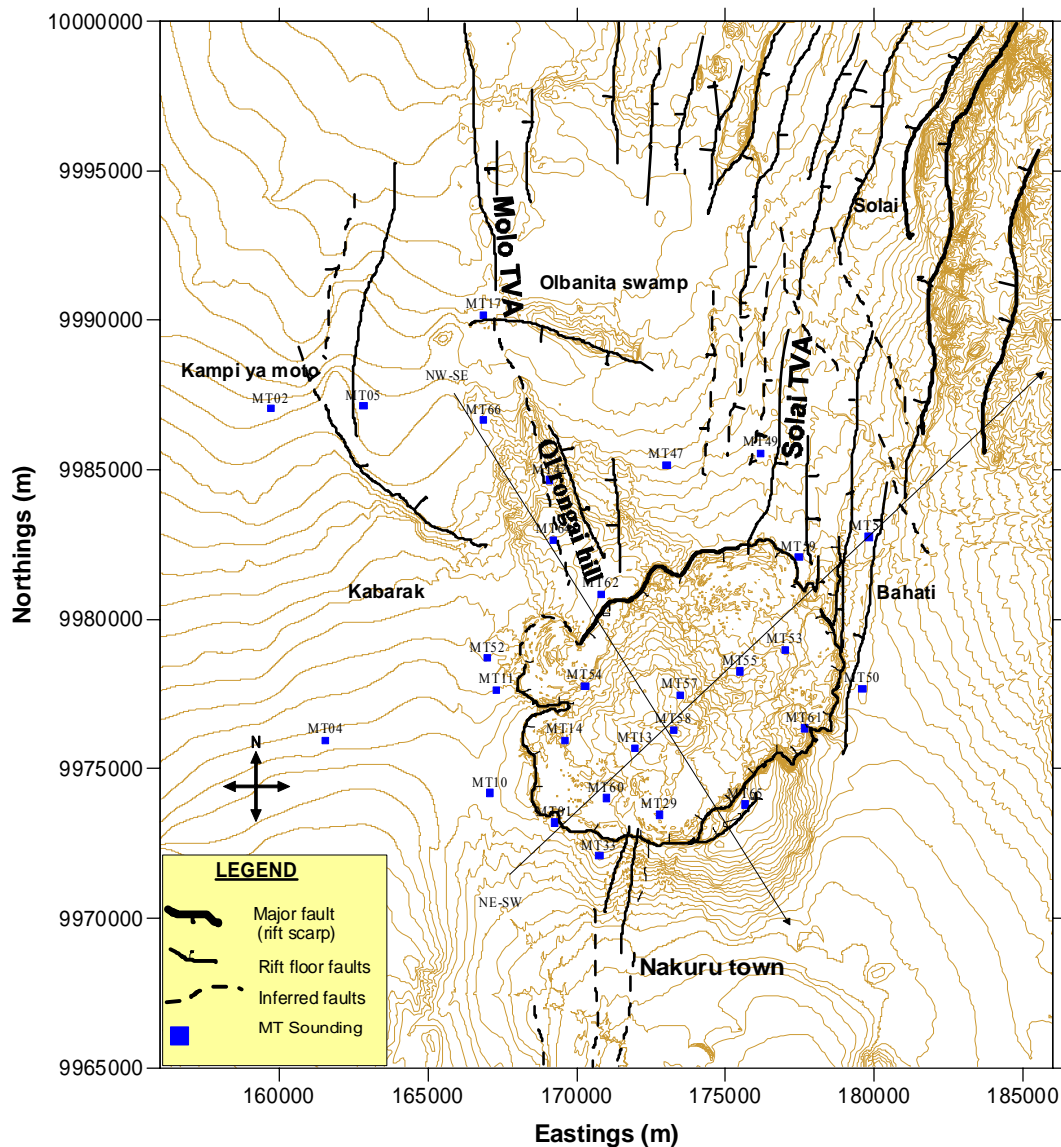


FIGURE 16: Map showing location of MT soundings and resistivity cross-sections

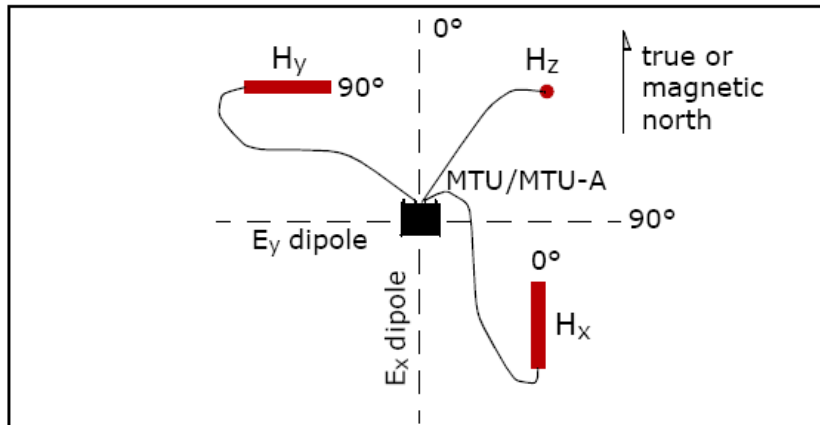


FIGURE 17: Field array for a 5-channel MT data acquisition system (Phoenix Geophysics Ltd, 2003)

about 21.5 hrs), and is suitable for shallow and deeper investigations. One of the 5-channel units was installed at a fixed location, about 30 km from Menengai caldera (which was the main area of focus), and was used as a remote-reference station for the other two data acquisition systems. This kind of array takes advantage of the fact that electromagnetic noise from the power line (50 or 60 Hz) and human activities tends to vary considerably over distance,

whereas the natural magnetic signal tends to be the same over large distances; the lower the frequency, the less variation.

Since the instruments are synchronized to Co-ordinated Universal Time (UTC) via signals from the Global Positioning System (GPS) satellites, low-noise time-series data acquired from the remote reference station were processed in combination with data from the other stations (acquired simultaneously) to reduce the effects of local noise and improve the quality and reliability of the survey results.

### 5.3.1 Data processing and interpretation

Time-series data downloaded from the the MTU-5A units were viewed using the program SyncTSV. This program allows viewing and printing of graphical representations of the raw time-series data, power spectra derived from the time-series data and coherence between pairs of orthogonal channels. Using the program SSMT2000, provided by Phoenix Geophysics-Canada (Phoenix Geophysics, 2003), Fourier transforms were produced from the raw time-series data. Fourier coefficients were then reprocessed using data from the reference site to filter out noise-affected data. The cross-powers were stored in files and could be displayed graphically using the program, MTU-Editor. Those files were then converted to industry-standard EDI format for use with WinGLink, geophysical interpretation software (from Geosystem).

TEM data (averaged stacks from GDP-16, TEM raw data) collected at the same locations as the MT site were also exported to the WinGLink program, where their 1-D models were used for static shift corrections on the MT data. The WinGLink program was used for 1-D inversion of the MT data. Appendix II shows an example of interpretation of MT data.

## 6. RESULTS OF THE TEM AND MT SURVEY

### 6.1 General discussion

The resistivity structure of high-temperature geothermal systems is generally characterized by a low-resistivity cap at the outer margins of the reservoir, underlain by a more resistive core towards the inner part. This structure has been found in both freshwater systems as well as brine systems, with the latter having lower resistivity values. Comparison of this resistivity structure with data from wells has been carried out in high-temperature geothermal fields, in Iceland (Árnason et al., 2000) and in the

Asal Rift (Djibouti, East Africa) (Árnason et al., 1988). The results have shown a good correlation with alteration mineralogy.

As discussed in Section 2.5, the resistivity is relatively high in cold unaltered rocks outside the reservoir and rather low at temperatures of 50-100°C as alteration intensity is normally low in this temperature range. At temperatures of 100-220°C, low-temperature zeolites and the clay mineral smectite are formed that have high conductivity. In the temperature range from 220 to about 240-250°C, the zeolites disappear and smectite is transformed into chlorite, forming the transition from the low-resistivity cap to the more resistive core. At about 240-250°C the smectite disappears and the resistive chlorite becomes the dominant mineral. This observation is of great importance, because the temperature dependence of the alteration mineralogy makes it possible to interpret the resistivity layering in terms of temperature, provided that the temperature is in equilibrium with the dominant alteration mineral.

The purpose of this research is to analyse TEM and MT data that had been collected in the Menengai geothermal prospect to study its resistivity structure in order to delineate the reservoir area, its heat source and possible up-flow zones. All the TEM soundings and used MT soundings together with the inversion models are published as special appendices to this report (Wameyo, 2005). The TEM resistivity structure of Menengai prospect is presented in 12 resistivity cross-sections crossing major geological structures, as well as by 2 iso-resistivity maps at different elevations with respect to sea level. The location of the resistivity cross-sections is shown in Figure 15.

## 6.2 TEM cross-sections

*Resistivity cross-section EW-2* (Figure 18) at the northern border of Menengai caldera shows a low-resistivity cap, an anomaly defined with resistivities  $<10 \Omega\text{m}$  over higher resistivity. The low-resistivity cap reaches an elevation of about 1900 m a.s.l. at sounding (TEM12) approximately 3000 m west of the caldera rim. The low-resistivity cap dips to the east and is at 1500 m a.s.l. below the eastern part of the caldera. To the west there is an indication of sloping down, but there is only one sounding (TEM58) to confirm that. The low-resistivity cap is underlain by a high-resistivity core, doming up to an elevation of 1750 m a.s.l. in sounding TEM12. The high-resistivity core dips clearly to the west, confirming the indication of a westward dip in the low-resistivity cap mentioned above. The high-resistivity core slopes down to the east and is not seen at 1300 m a.s.l. within the central part of the caldera. However, in the easternmost part of the caldera a high-resistivity body is seen at 1400 m a.s.l. in sounding TEM09. This will be commented upon later.

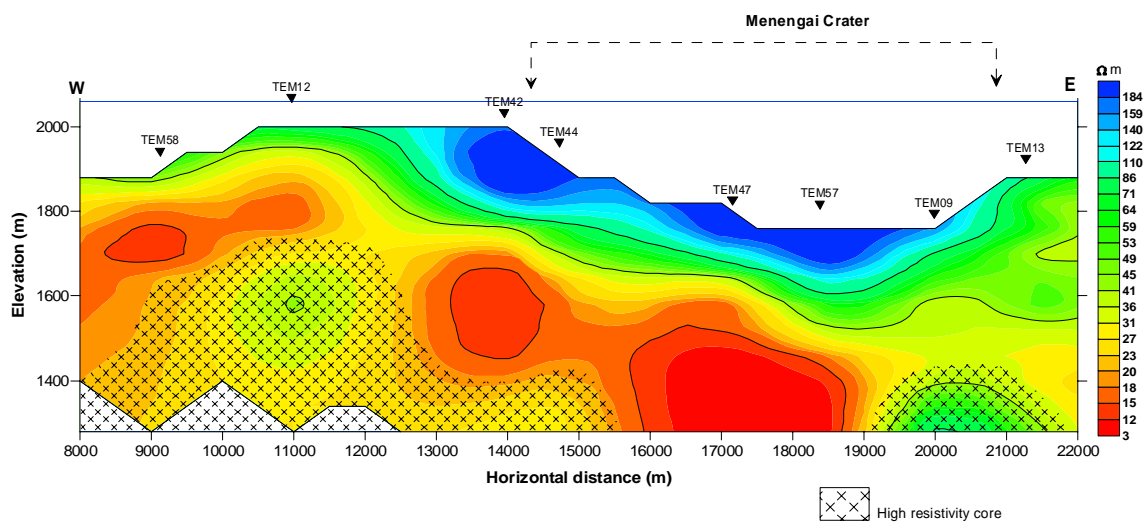


FIGURE 18: TEM resistivity cross-section EW-2

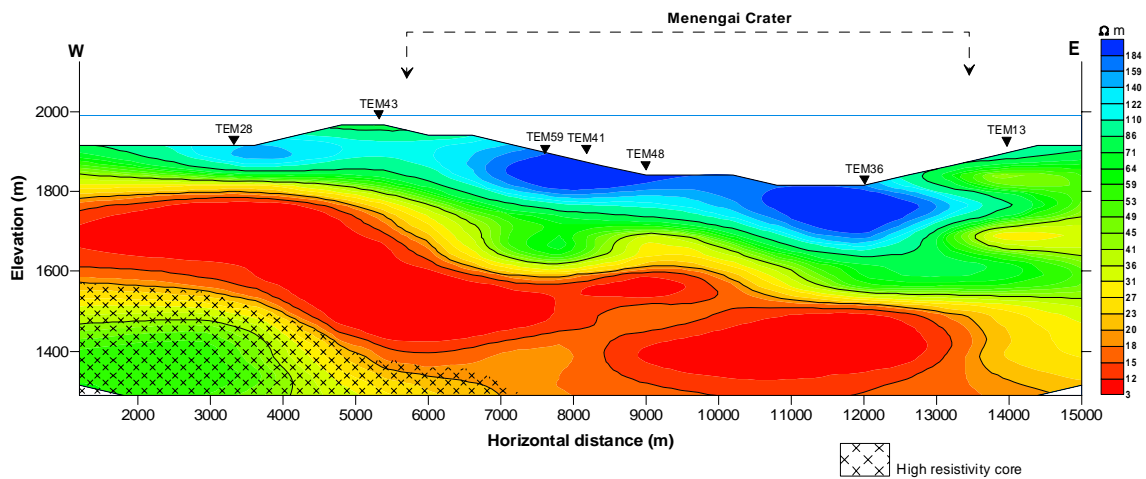


FIGURE 19: TEM resistivity cross-section EW-3

*Resistivity cross-section EW-3* (Figure 19) cuts across the caldera 2 -3 km to the south of EW-2. It reveals a low-resistivity cap over a high-resistivity core. The low-resistivity cap is observed at an elevation of 1800 m a.s.l. in the westernmost sounding (TEM28). It slopes to the east but there is no indication of sloping to the west in this section. A high resistivity core is seen in the western part of the cross-section, reaching an elevation of almost 1600 m a.s.l. in sounding TEM28 sloping down to the east.

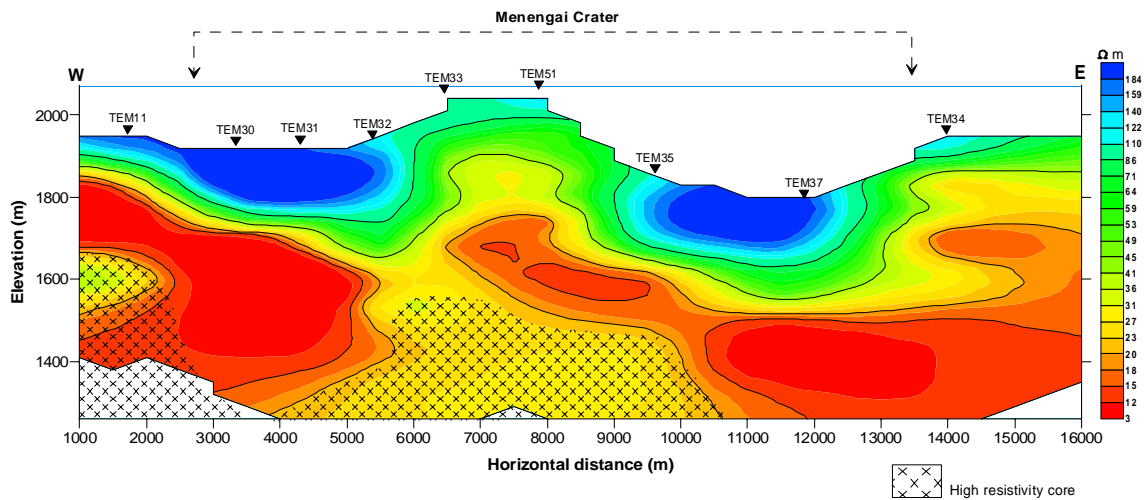


FIGURE 20: TEM resistivity cross-section EW-4

*Resistivity cross-section EW-4* passes right across the caldera (Figure 20). It clearly defines a low-resistivity cap over a high-resistivity anomaly in the northwest part of the caldera. The low-resistivity cap reaches an elevation of approximately 1800 m a.s.l. in the westernmost sounding (TEM11), and then shows gradual sloping to the east along the cross-section. There is an indication of the low-resistivity cap doming up in the easternmost sounding (TEM34) but that cannot be confirmed as more soundings are needed for that. The high-resistivity core anomaly is sloping well on both sides, defining boundaries within this profile. An interesting feature is the upward doming of the low-resistivity cap almost to the surface in soundings in the middle of the caldera (TEM54 and 33) where surface manifestations are observed.

*Resistivity cross-section EW-5*, across the caldera (Figure 21), shows the low-resistivity cap across the section. It is close to the surface to the west and east of the caldera, but at greater depth within it. The low resistivity is underlain by higher resistivity in the western part and west of the caldera.

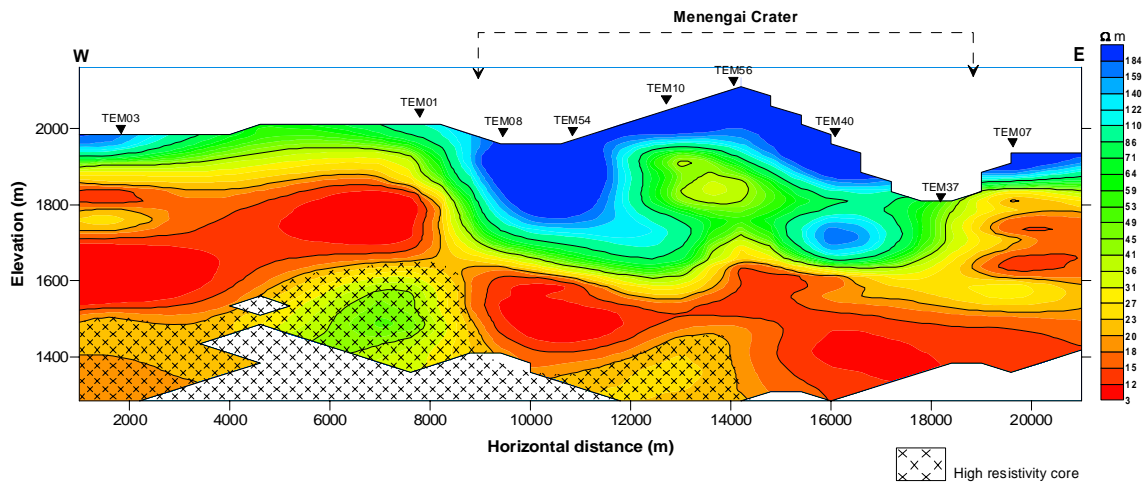


FIGURE 21: TEM resistivity cross-section EW-5

Resistivity cross-section EW-6 crosses the southern part of caldera (Figure 22) showing low resistivity sloping down to the east as the cross-sections reach the southern part of the caldera. Higher resistivity is seen at depth under the caldera indicating that the cross-section is close to the southern margin of the reservoir.

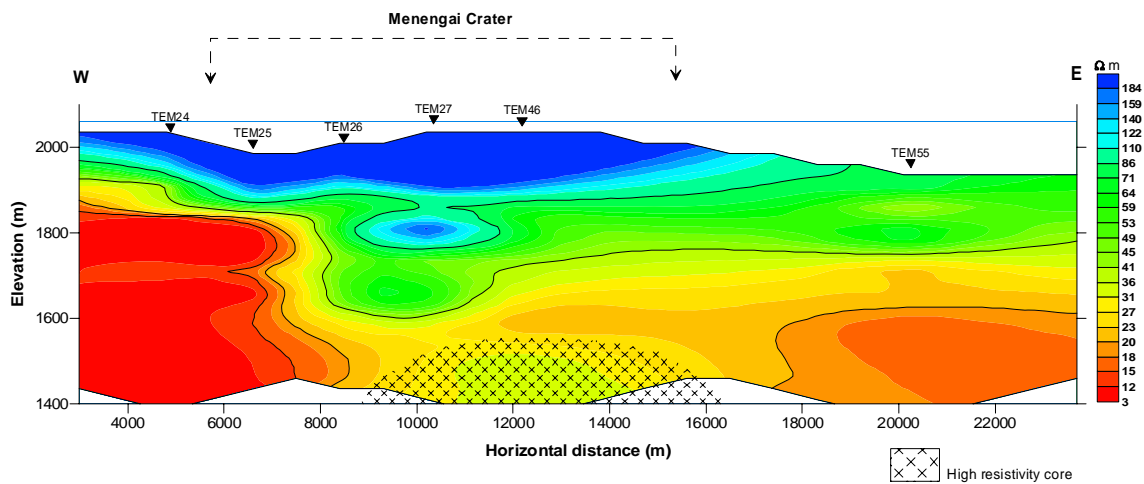


FIGURE 22: TEM resistivity cross-section EW-6

Resistivity cross-section EW-7, Figure 23, shows a clear thickening of the low resistivity in the western part, indicating that the cross-section cuts the cap as it slopes down to the south. A high resistivity body is seen at depth. The cross-section confirms, as seen in EW6, that it is close to the southern margin of the reservoir.

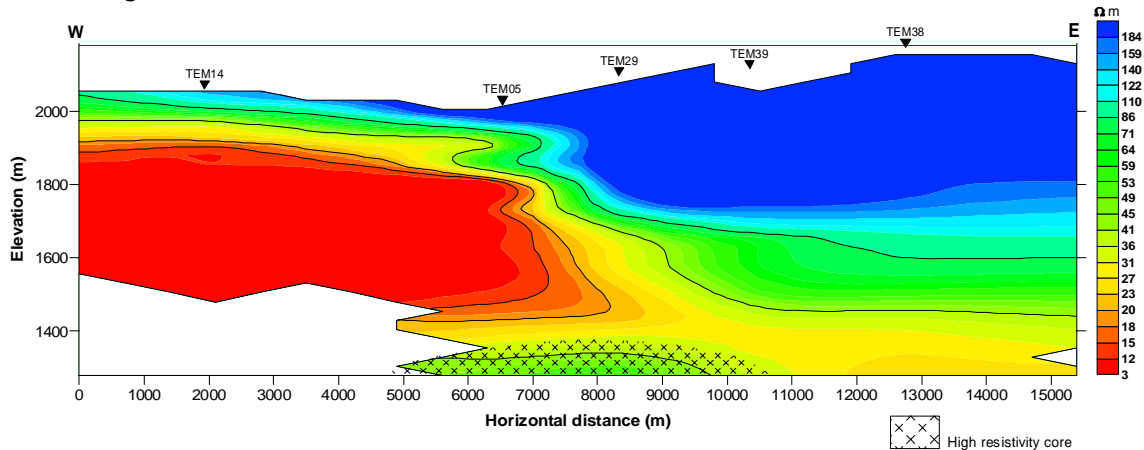


FIGURE 23: TEM resistivity cross-section EW-7

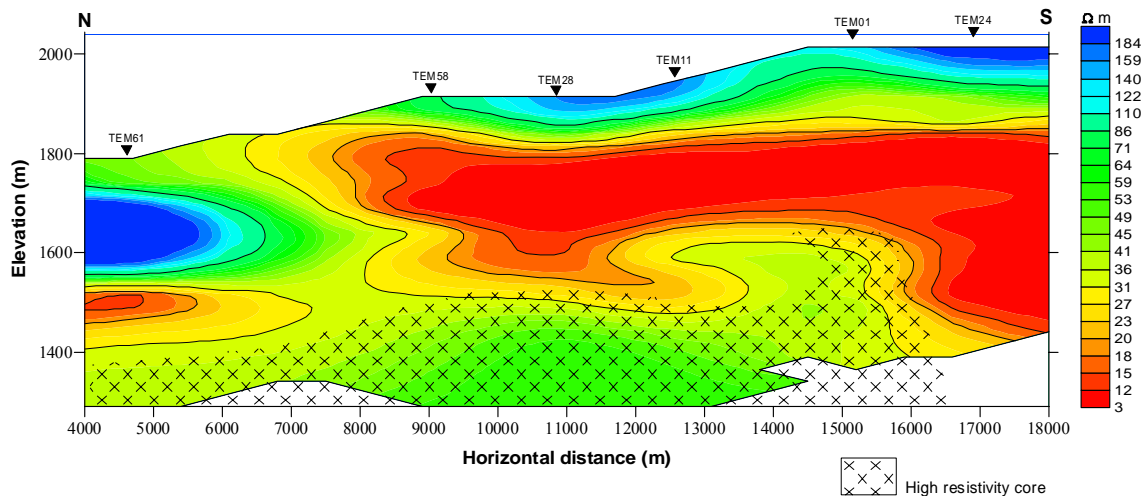


FIGURE 24: TEM resistivity cross-section NS-1

*Resistivity cross-section NS-1* is a north-south bound resistivity cross-section, passing west of the caldera (Figure 24). It shows a low-resistivity layer sloping down to the north. It is underlain by higher resistivity except in the far south.

*Resistivity cross-section NS-2*, (Figure 25) crosses the western edge of Menengai caldera and Ol rongai hill to the north. The cross-section shows high resistivity at a shallow depth within the caldera and a continuous low-resistivity layer at depth. This low-resistivity cap is shallower to the north, at about 1800 m a.s.l., and the northern limit is not seen as there is no data farther north of this profile. In the northern part the low resistivity is underlain by higher resistivity, dipping to the south. Where the low resistivity is closest to the surface in the northern part, there is fumarole activity along Ol rongai hill.

*Resistivity cross-section NS-3*, (Figure 26) passes right through the middle of the caldera and has a low-resistivity cap that opens to the north but slopes down to the south in the northern part of the caldera (between TEM44 and TEM59). The high-resistive core is deeper (at 1550 m a.s.l.) in this profile compared to NS-2 (1650 m a.s.l.), immediately to the west. This shows that a boundary is approached as we move further east. It is interesting to note the extension of the low-resistivity cap up to the surface in the middle of the caldera, just underneath surface manifestations.

*Resistivity cross-section NS-4* that also cuts through the caldera on the eastern side (Figure 27) shows a thick low-resistivity layer under and north of the caldera (below TEM60) and south (TEM40). Signs of the approaching of a boundary to the east are confirmed by the high-resistivity core below this cap that is at deeper levels (1400 m a.s.l.) when compared to NS-1 and NS-2.

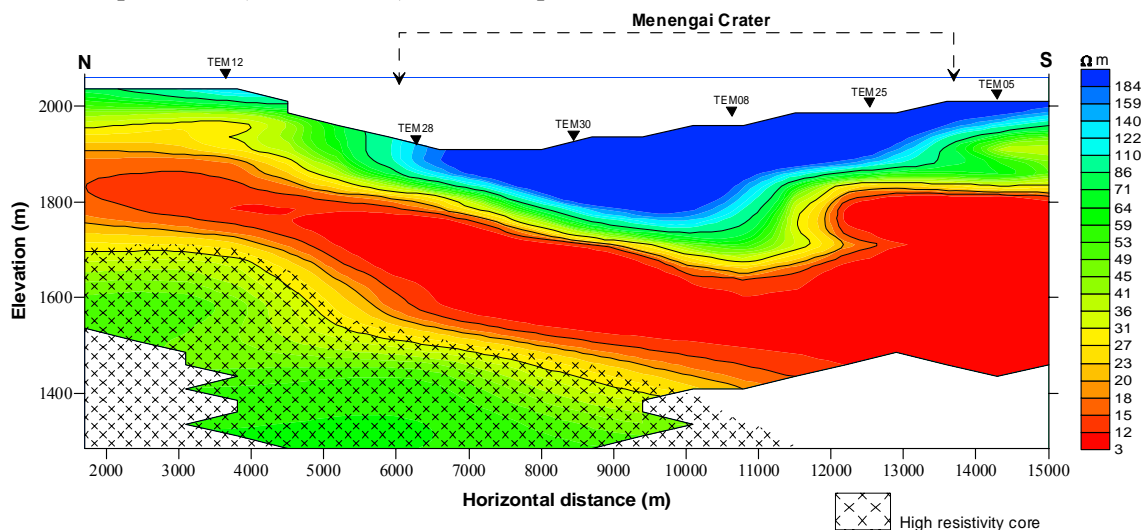


FIGURE 25: TEM resistivity cross-section NS-2

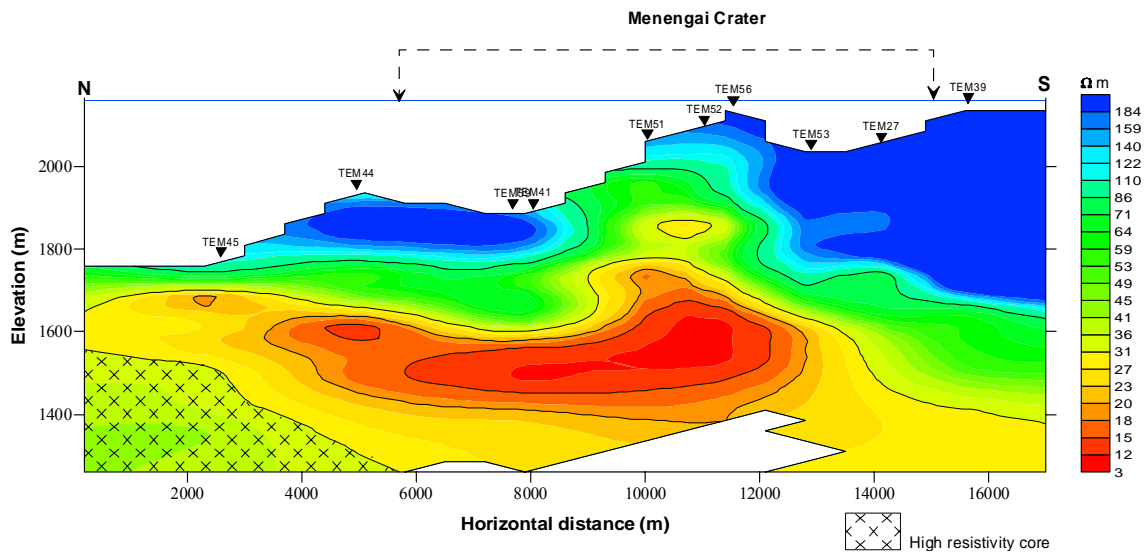


FIGURE 26: TEM resistivity cross-section NS-3

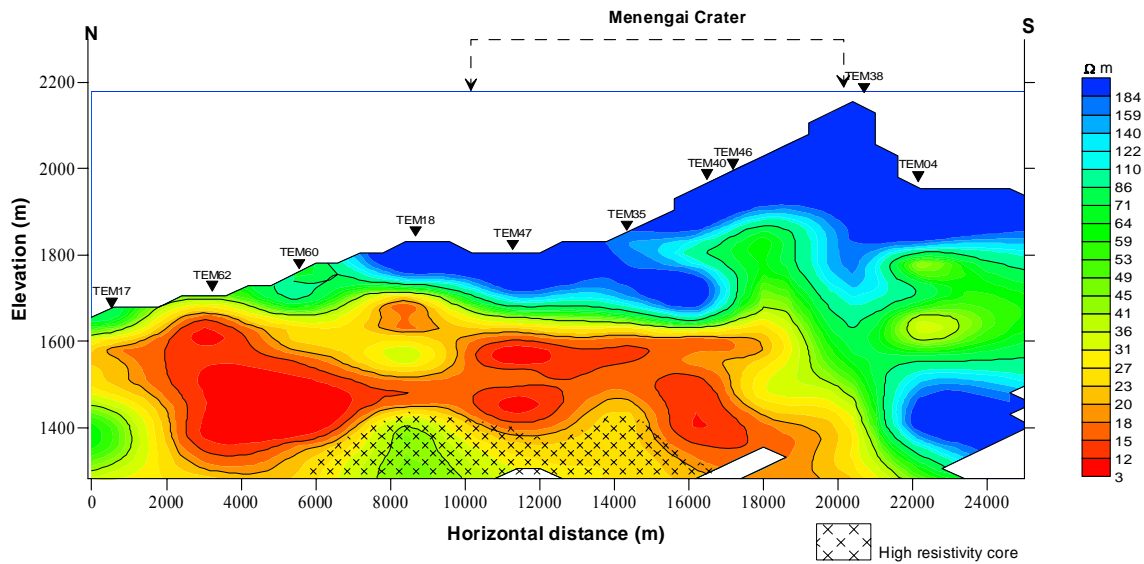


FIGURE 27: TEM resistivity cross-section NS-4

Resistivity cross-section NW-SE passes through the caldera and Ol ronga to the northwest (Figure 28) and has a thick low-resistivity layer or cap (TEM38 – TEM51) over a deep high-resistivity core that is seen in the northwest (below TEM61) marking the southeastern margin of the system. The low-

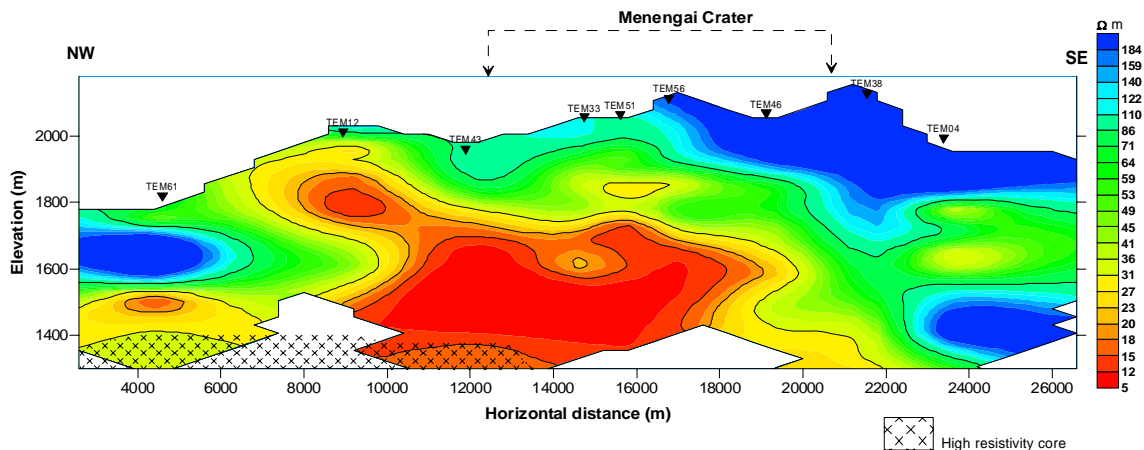


FIGURE 28: TEM resistivity cross-section NW-SE

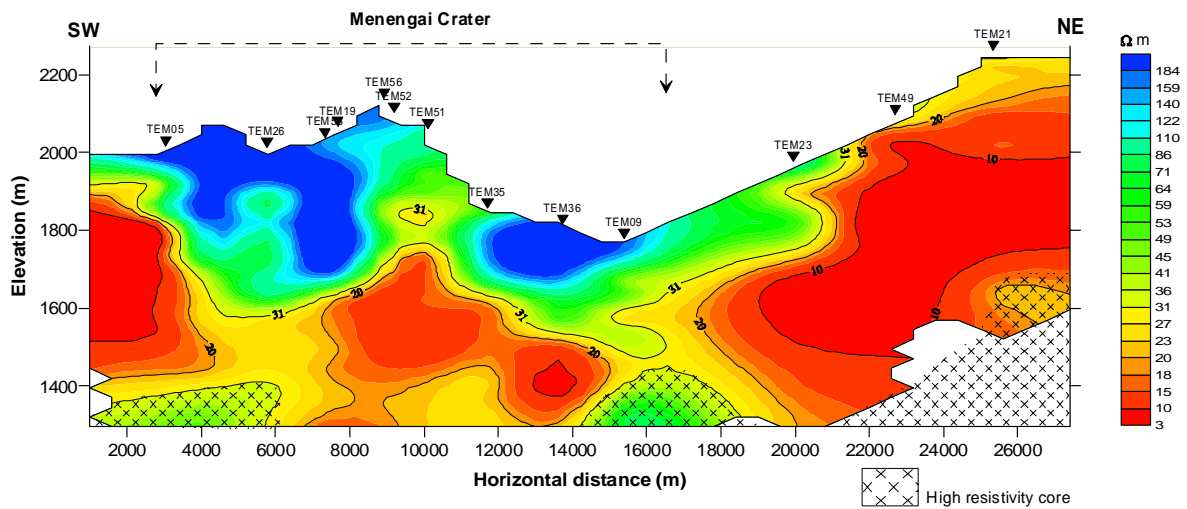


FIGURE 29: TEM resistivity cross-section NE-SW

resistivity cap in this profile is at shallow levels below TEM12, at about 1850 m a.s.l., but deepens to the northwest. Surface manifestations are observed around TEM12, where the low-resistivity cap is closest to the surface.

*Resistivity cross-section NE-SW* also passes through the caldera in the Bahati area (Figure 29). A thick low-resistivity cap over a deep resistive core, below 1400 m a.s.l., at the southwest end of this section marks the southern margin of the anomaly observed in the western area of the caldera from previous resistivity sections. To the northeast, the low-resistivity cap deepens until we get to TEM36 where emergence of yet another system is observed below TEM09 with the emergence of a new high-resistivity body. Further to the northeast the low-resistivity layer reaches elevation of approximately 2000 m a.s.l. For clarification, this system will here be called the Solai-system.

### 6.3 TEM resistivity maps

The results of the survey are also presented as iso-resistivity maps showing resistivity at a certain depth.

*Iso-resistivity map at 1800 m a.s.l.* (Figure 30), cuts through the top of the low-resistivity cap where it reaches the highest elevation just west of the Menengai caldera. Due to insufficient data in the area west of the caldera the area is “open” to the west. The low resistivity in the northeast shows the top of the low-resistivity cap covering the Solai system. The indication of the Solai geothermal system, is only

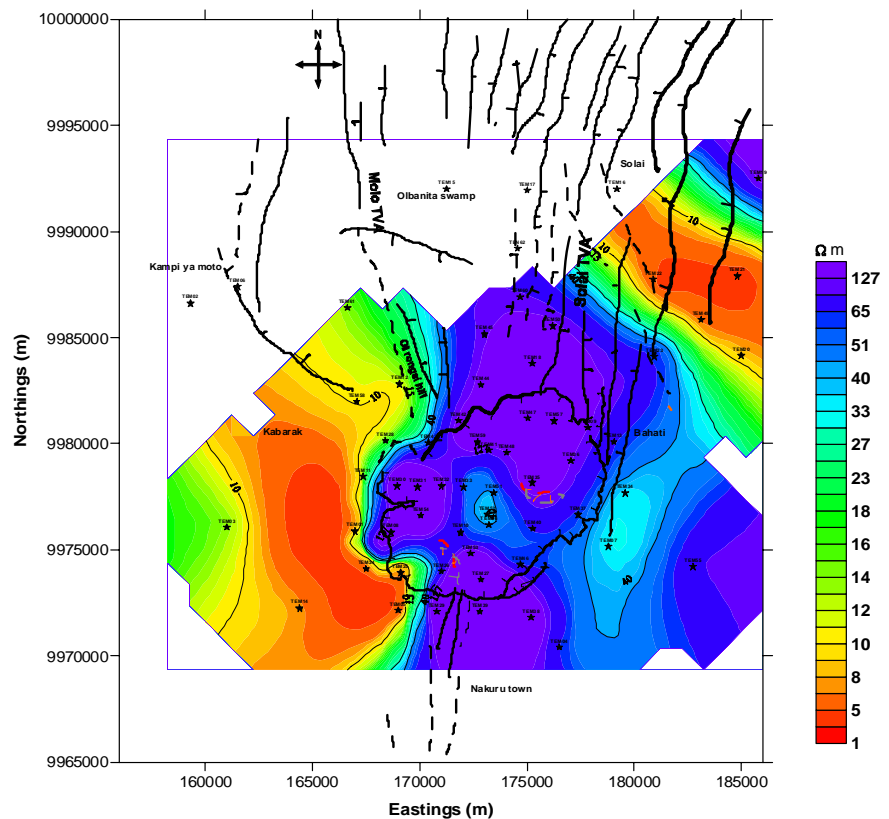


FIGURE 30: TEM resistivity distribution at 1800 m a.s.l.

founded by a few soundings in the northeastern part of the survey area. High resistivity ( $> 200 \Omega\text{m}$ ) is observed within most parts of the Menengai caldera related to the unaltered young lava flows that cover most parts of the caldera and its environs at shallow levels.

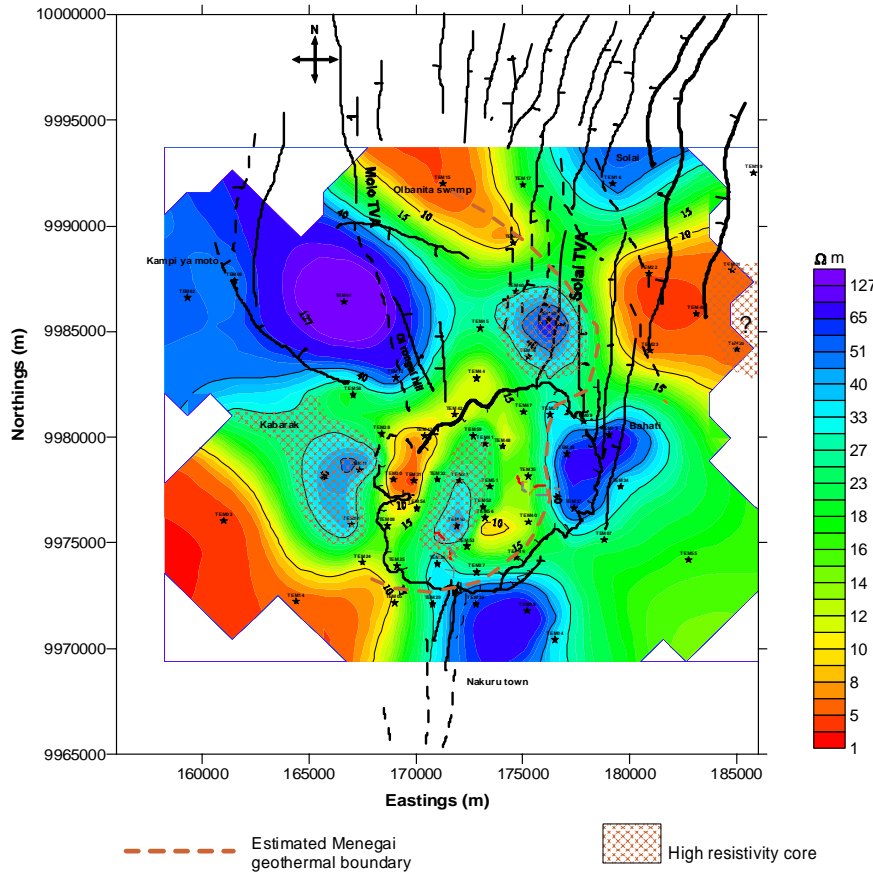


FIGURE 31: TEM resistivity distribution at 1600 m a.s.l.

*Iso-resistivity map at 1600 m a.s.l., at an average 400 m depth from surface (Figure 31), cuts the low-resistivity cap of the Menengai system as it slopes down towards north and south. The map cuts the top of the high-resistivity core within the caldera and northwest of the caldera. Here it is clear that the Menengai geothermal system extends to the northwest outside the survey area. The high resistivity in the eastern part of the caldera reflects rocks outside the geothermal reservoir, not affected by thermal alteration. Northeast is not well defined due to insufficient data coverage but soundings east of Solai show a clear evidence of the anomaly that has been referred to as the Solai system.*

### 6.4 MT results

*MT resistivity cross-section NE-SW, shown in Figure 32, passes right through the middle of Menegai caldera along its main axis. A low-resistivity anomaly is seen along the whole profile at 0.5-1 km*

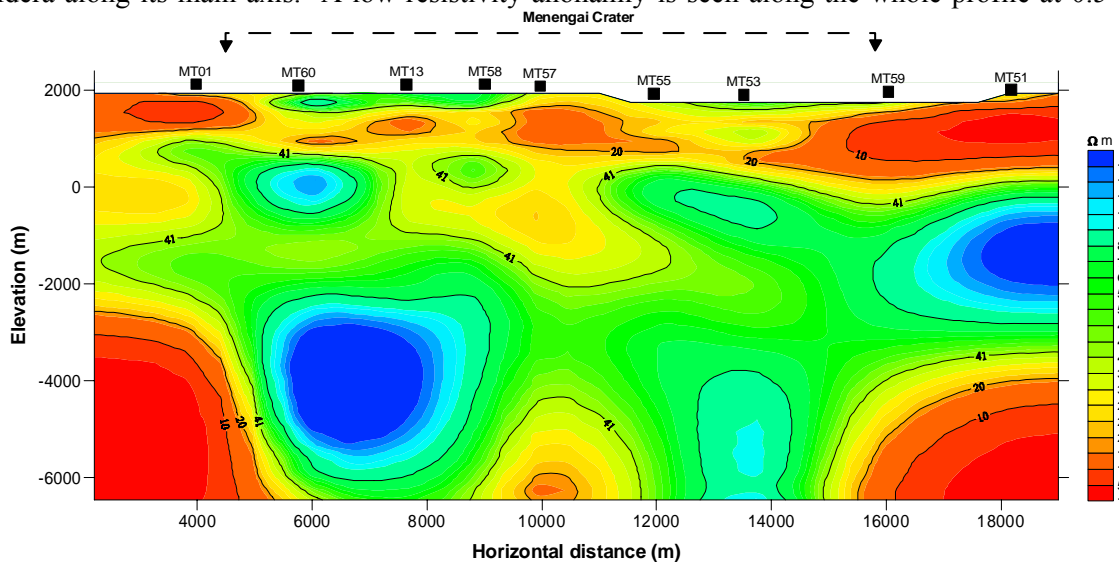


FIGURE 32: MT resistivity cross-section NE-SW

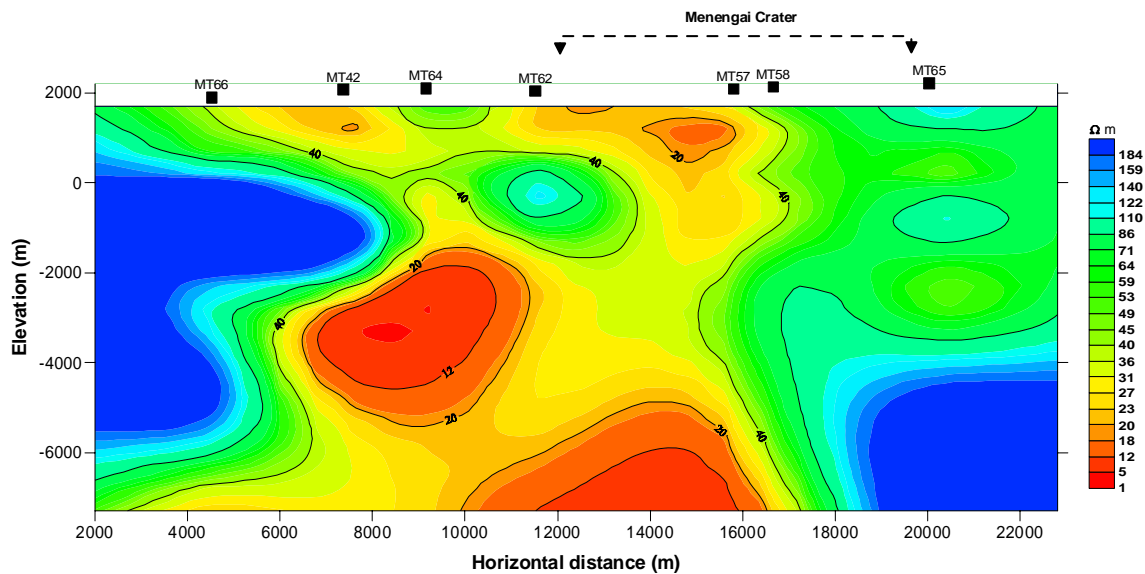


FIGURE 33: MT resistivity cross-section NW-SE

depth, with the lowest resistivity to the southwest ( $< 10 \Omega\text{m}$ ) and the northeast ( $< 10 \Omega\text{m}$ ). This anomaly is also seen in the TEM data as shown in Figure 29. Another low-resistivity body is observed inside the caldera at about 8 km depth and two others at each side of the profile, at about 6-7 km depth. Those deeper low-resistivity bodies are not well defined by the available data.

*MT resistivity cross-section NW-SE* passes through the caldera and Ol ronga hill and is shown in Figure 33. A broad (10 km) low-resistivity zone is observed in the northwest part of the caldera extending some 6 km to the northwest from the caldera rim. It is at about 3-4 km depth in the northwest but deepens to the southeast inside the caldera where it is at about 6 km depth. It depicts an anomaly of relatively low resistivity.

## 6.5 Resistivity structure of the Menengai geothermal prospect area from TEM and MT results

This resistivity survey is a first step in a geothermal investigation of the Menengai geothermal system. From the TEM and MT results, the Menengai prospect appears to host a large geothermal system that extends from Solai to areas north and south of the caldera (Figure 31). The results of the survey indicate the Menengai geothermal system being much larger than anticipated. Based on the resistivity data it may exceed  $150 \text{ km}^2$  at 1300 m a.s.l. in planar view. However, a more extensive survey is needed to delineate the system in details.

Due to inadequate data outside the caldera, the boundaries of the main resistivity structures are not well defined to the west and north. The eastern margin cuts the southwestern flank of the Menengai caldera, SW-NE, at about 1300 m a.s.l., but due to insufficient data coverage no boundaries are to be seen to the northwest. The low-resistivity cap slopes down in all directions except to the northwest, giving a good view of the shape of the southeastern part of the system.

The intersections of major structures such as the Molo and Solai tectonic axis with the caldera and other structures that run along the rift floor (Figure 31) appear to have a strong influence on resistivity distribution in this prospect area, observed in the MT results. MT resistivity cross-sections show low resistivity at depth that could be related to heat sources for the geothermal systems defined by TEM at shallower depths.

## 7. CONCLUSIONS AND RECOMMENDATIONS

- The Menengai geothermal system exceeds 150 km<sup>2</sup> at 1300 m a.s.l. as defined by resistivity structures.
- A low-resistivity cap delineates the geothermal system, showing boundaries in all directions except northwest.
- The low-resistivity cap is underlain by a high-resistivity core that reaches an elevation of approximately 1750 m a.s.l. close to the northeastern caldera rim.
- The existence of a high-resistivity core indicates reservoir temperatures exceeding 240-250°C, provided there is an equilibrium between the temperature in the reservoir and the alteration of the rocks, as expressed by the resistivity.
- Soundings in the northeast part of the survey area indicate the existence of another geothermal system, the Solai system. A more extensive survey is needed to verify that and to delineate it.
- MT resistivity cross-sections show low resistivity at deeper levels that could be related to heat sources.
- Major geological structures appear to have a strong influence on the resistivity distribution in this prospect area, as observed in the MT results.

The Menengai prospect appears to host a large geothermal system that can be developed to boost Kenya's power demand. This field could be defined better if more TEM and MT soundings were done west and north of the prospect. Additional soundings inside the caldera will also fine-tune the picture inside the caldera, especially in areas where the low-resistivity cap is not well defined due to large data spacings.

The experience during prospecting for geothermal resource in Menegai area proved that using both TEM and MT has proven to be very quick and effective in exploring for geothermal resources. The sensitivity of electromagnetic methods to low resistivity makes it easier for TEM to define thickness and depth of low-resistivity caps that are common in high-temperature geothermal systems. MT, on the other hand, is handy in locating and defining deep resistivity anomalies such as low resistivity associated with thermal excitation of conduction in the massive crystalline rock comprising the basement.

## ACKNOWLEDGEMENTS

I wish to express my sincere gratitude to KenGen for the chance and support to participate in this training. Also to Martin Mwangi, Silas Simiyu, Zack Muna, Nicholas Mariita, Stephen Onacha and the entire KenGen geophysics staff for support during my preparation for the course. I wish to thank our human resources staff Mrs. Beatrice Soy, Mary Gachuhi, Suzy Ogwaye and Matthew Chebogel for their assistance and support in granting me study leave and getting necessary travelling documents.

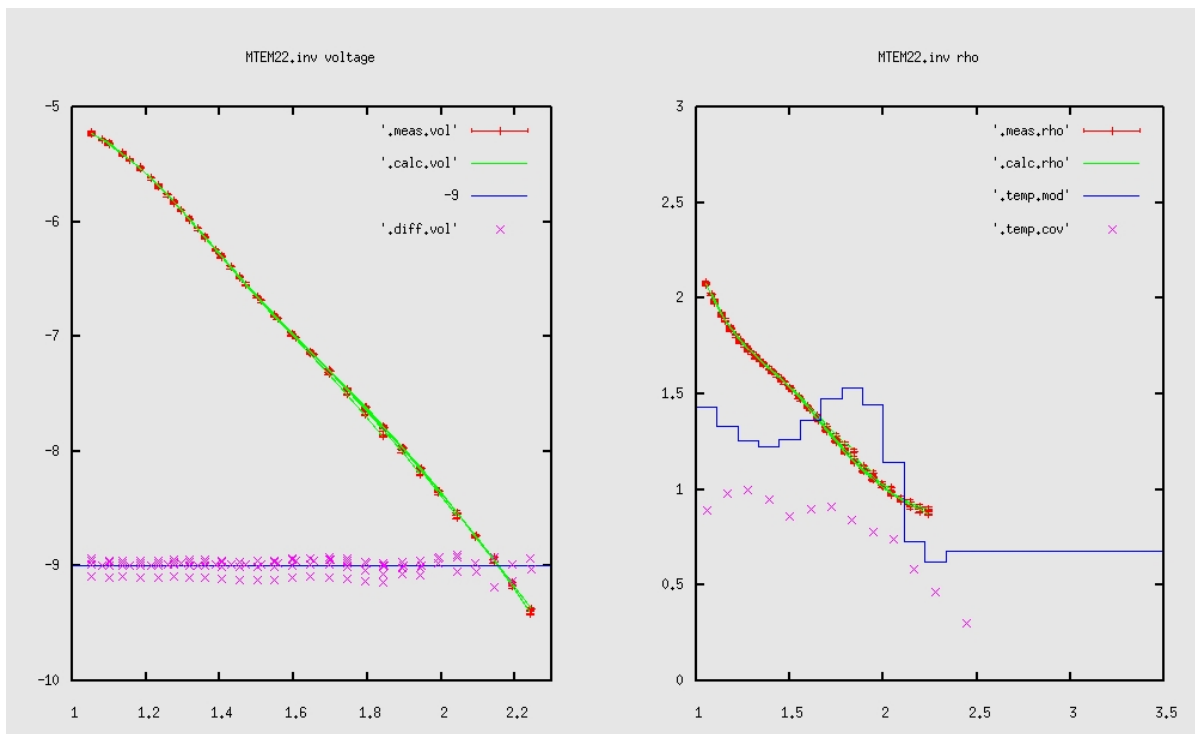
To the UNU, I am very grateful for the financial support and the rare opportunity that you have generously given me to gain wonderful knowledge from this course. I wish to express my unreserved appreciation to the UNU-GTP staff, Dr. Ingvar B. Fridleifsson (Director), Mr. Lúdvík S. Georgsson (Assistant director) and Mrs. Guðrún Bjarnadóttir for making our stay in Iceland comfortable and for the superb coordination of all our training activities and excursions. I am greatly indebted to my supervisors, Knútur Árnason assisted by Dr. Hjálmar Eysteinnsson and Ragna Karlsdóttir, who are part of ISOR's geophysics team, for their guidance, sharing knowledge and experience with me, not to mention the encouragement they constantly gave me during my specialized course and project write-up. I feel honoured to have been your student.

Finally, I wish to thank my wife, Phoebe Agufa and my sons, Phillip Wameyo and Pascal Mudave for enduring my absence, for their encouragement and support. May God bless you and grant you your wishes and happiness in life.

## REFERENCES

- Archie, G.E., 1942: The electrical resistivity log as an aid in determining some reservoir characteristics. *Tran. AIME*, 146, 54-67.
- Árnason, K., 1989: *Central loop transient electromagnetic sounding over a horizontally layered earth*. Orkustofnun, Reykjavík, report OS-89032/JHD-06, 129 pp.
- Árnason, K., Björnsson, G., Flóvenz, Ó.G., and Haraldsson, E.H., 1988: *Geothermal resistivity survey in the Asal Rift in Djibouti*. Orkustofnun, report OS-88301/JHD-05 prepared for UND-OPS and ISERT, vol. I, 48 pp.
- Árnason, K., Karlsdóttir, R., Eysteinnsson, H., Flóvenz, Ó.G., and Gudlaugsson, S.Th., 2000: The resistivity structure of high-temperature geothermal systems in Iceland. *Proceedings of the World Geothermal Congress 2000, Kyushu-Tohoku, Japan*, 923-928.
- Cagniard, L., 1953: Basic theory of the magneto-telluric method of geophysical prospecting. *Geophysics*, 18, 605-635.
- Dakhnov, V.N., 1962: *Geophysical well logging*. Q. Colorado Sch. Mines, 57-2, 445 pp.
- Geonics Ltd, 1980: *Application of Transient Electromagnetic techniques*. Geonics Ltd., Technical note NT-17.
- Hersir, G.P., and Björnsson, A., 1991: *Geophysical exploration for geothermal resources. Principles and applications*. UNU-GTP, Iceland, report 15, 94 pp.
- ISL, Michigan State University, 1999: *Liquid molding*. ISL, Michigan State University, webpage [islnotes.cps.msu.edu/trp/rtn/modl\\_mes.html](http://islnotes.cps.msu.edu/trp/rtn/modl_mes.html).
- Jones, A.G., 1988: Static shift of magnetotelluric data and its removal in a sedimentary basin environment. *Geophysics*, 53-7, 967-978
- Keller, G.V., and Frischknecht, F.C., 1966: *Electrical methods in geophysical prospecting*. Pergamon Press Ltd., Oxford, 527 pp.
- Morris, F.H., and Becker A., 2001: *Berkeley course in applied geophysics*. University of California, Berkeley, Ca, unpublished.
- Mungania, J., 2004: *Geological studies of Menengai geothermal prospect*. KenGen Ltd., internal report, 18 pp.
- Phoenix Geophysics, 2003: *V5 System 2000MTU/MTU-A User Guide*. Phoenix Geophysics, Ltd., Toronto.
- Quist, A.S., and Marshall, W.L., 1968: Electrical conductances of aqueous sodium chloride solutions from 0 to 800°C and at pressures to 4000 bars. *J. Phys. Chem.*, 72, 684-703.
- Wameyo, P.M., 2005: *Appendices to the report: Magnetotelluric and Transient Electromagnetic methods in geothermal prospecting, with examples from Menengai, Kenya*. UNU-GTP, Iceland, Report 21 appendices, 26 pp.
- Ward, S.H., and Wannamaker, P.E., 1983: *The MT/AMT Electromagnetic method in geothermal exploration*, UNU-GTP, Iceland, report 5, 107 pp.

**APPENDIX I: TEM 1-D modelling using CLTINV**



**APPENDIX II: MT 1-D modelling**

